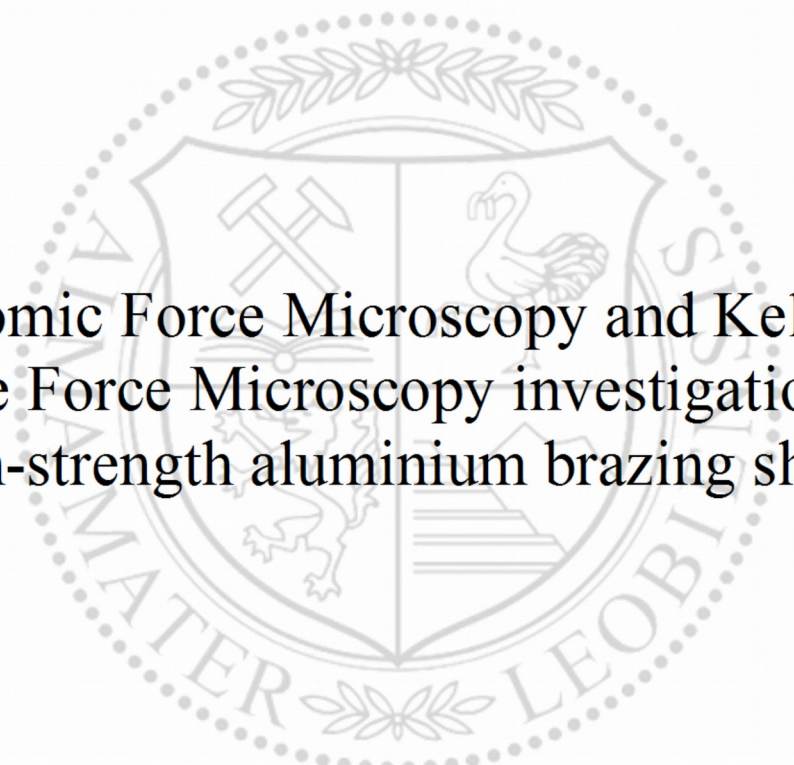




Institute of Physics

Master's Thesis



Atomic Force Microscopy and Kelvin  
Probe Force Microscopy investigations of  
high-strength aluminium brazing sheets

Michael Huszar, BSc

September 2019

under supervision of

Univ.-Prof. Dr. Christian Teichert,  
Institute of Physics

Dr. Markus Kratzer,  
Institute of Physics

Dr. Thomas Kremmer,  
Chair of Nonferrous Metallurgy

refereed by

Univ.-Prof. Dr. Christian Teichert

dedicated to my parents



## EIDESSTATTLICHE ERKLÄRUNG

Ich erkläre an Eides statt, dass ich diese Arbeit selbständig verfasst, andere als die angegebenen Quellen und Hilfsmittel nicht benutzt, und mich auch sonst keiner unerlaubten Hilfsmittel bedient habe.

Ich erkläre, dass ich die Richtlinien des Senats der Montanuniversität Leoben zu "Gute wissenschaftliche Praxis" gelesen, verstanden und befolgt habe.

Weiters erkläre ich, dass die elektronische und gedruckte Version der eingereichten wissenschaftlichen Abschlussarbeit formal und inhaltlich identisch sind.

Datum 14.09.2019

*Huszar Michael*

---

Unterschrift Verfasser/in  
Michael, Huszar  
Matrikelnummer: 00635113

# Acknowledgments

Over the development of this work, i have met many people whom i would like to express my gratitude.

First to **Univ.-Prof. Dr. Christian Teichert**, for beeing a kind and understanding supervisor, introducing me to the wide field of scanning probe microscopy and giving me the oportunity to work with the SPM Group Leoben. Also for the chance to write this thesis and the many hours which was necessary for the correction of this work.

To **Dr. Markus Kratzer**, who explained to me, in understanding terms, the ups and downs of the KPFM technique and AFM in general. Who also lost many hours correcting my formating and spelling failures and giving me good advice whenever it was possible.

To **Dr. Thomas Kremmer**, who initated this work and whithout whom it couldn't have taken place. Who had an open ear for all material-specific questions and had to endure my original script as first proofreader.

To **Univ.-Prof. Dr. Helmut Antrekowitsch** who was so kind to correct some parts in the last minute.

To **Anatol Drilicek**, who introduced me to phyton and was there for me, whenever i got some parts of the codes wrong, and didn't laugh at my complicated approach to some problems.

To **Heide Kirchberger**, for administrative support, and an open ear for many problems.

To my **friends** and **colleagues**, who had to endure me in this quite long and hard time. Who tried to give me good advise, even when i wasn't listening and where by my side, when i needed them most.

And last, but by no means least, to my **parents**, who were there for me and supported me from the beginning, who gave me as much strength as they could spare, and even a little more.

**Thank you.**

## Abstract

Aluminium and its alloys are excellent materials for lightweight constructions and transportation applications (due to their low density around of  $2.7 \text{ g/cm}^3$ ). In addition, the combination of high thermal conductivity (205 to  $232 \text{ WK/m}$ ) with good corrosion resistance also make them especially suitable for heat exchangers in the automotive industry. For the development of these heat exchangers, multilayered brazing sheets with different aluminium alloys are used. Conventionally, these sheets consist of two layers where the core material (e.g. Al-Mn) provides the mechanical strength, and the brazing layer (e.g. Al-Si) with a lower melting point (e.g.  $575 \text{ }^\circ\text{C}$ ) is used to bond the final product together. To improve efficiency and service life, it is possible to change the core material to a high-strength Al alloy, although this may lead to an increased risk of corrosion.

In this work, two different high-strength Al brazing sheets are studied via Atomic Force Microscopy (AFM) and Kelvin Probe Force Microscopy (KPFM) to explore the physical parameters which influence the corrosion processes. The core material in both sheets is AlZn4.5Mg1 and the brazing layer is an eutectic AlSi10 alloy. These two layers have to be separated by an intermediate layer which prevents Si diffusion and subsequent loss of mechanical strength. The first investigated sample had a pure Al (with 99.85 wt%) intermediate layer and the second one an AlMn1 layer. Metallographic cross-sections of the sheets were prepared for the examination after a simulated brazing process (12 min at  $610 \text{ }^\circ\text{C}$ ). The investigation included the measurement of the brazed state by means of AFM and KPFM as well as the topographic change after immersion in a solution (42 g/l NaCl, adjusted to pH 3 with acetic acid) for fixed time intervals of 1 h and 3 h only via AFM. With a modified experimental setup, KPFM measurements were also possible for the AlMn1 sample after the immersion testing.

In both samples, the inclusions were found to have a more noble potential when compared with the surrounding Al-matrix. Al(Mn,Fe)Si-particles exhibited a potential difference of approximately 300 mV. Accurate values for the potential differences of smaller inclusions ( $< 2 \text{ } \mu\text{m}$ ) could not be determined, but a trend to higher potentials was identified. In the intermediate layers of the two samples, the inclusions were observed to be different. In the pure Al sample, a high number of very small inclusions (area of around  $3 \text{ } \mu\text{m}^2$ ) was observed. The size and number of these inclusions decreased upon increasing corrosion time. It was also possible to determine the alteration in the surface potential between the layers. Such change was more pronounced on the border of the intermediate layer to the core material ( $1.15 \text{ V}/\mu\text{m}$ ) and is a consequence of the diffusion processes during brazing.

Based on the results obtained from the performed measurements, the possibility of

estimating corrosion properties using the KPFM technique was demonstrated on the samples studied. Therefore, the methodology used in this work allowed the conclusion that AlMn1 as intermediate layer for high strength Al brazing sheets is the most appropriate candidate material to minimize the corrosion attack under the conditions studied here. The outcomes of this research work shed light on the possibility of further investigating the effects of particle size on the corrosion resistance of these lightweight materials.

## Kurzfassung

Aluminium und seine Legierungen sind ein ausgezeichneter Werkstoff für Leichtbau- und Transportanwendungen (wegen ihrer Dichte im Bereich von  $2.7 \text{ g/cm}^3$ ). Zudem macht die Kombination aus hoher Wärmeleitfähigkeit (205 bis  $232 \text{ WK/m}$ ) mit guter Korrosionsbeständigkeit Aluminium besonders für Wärmetauscher in der Automobilindustrie geeignet. Für den Bau dieser Wärmetauscher werden mehrschichtige Lotbleche mit verschiedenen Aluminiumlegierungen verwendet. Üblicherweise bestehen diese Bleche aus zwei Schichten, dem Kernmaterial (z.B. Al-Mn) für die mechanische Festigkeit und der Lotschicht (z.B. Al-Si) mit einem niedrigen Schmelzpunkt (z.B.  $575 \text{ °C}$ ) zum Verbinden des Endproduktes. Es ist möglich, das Kernmaterial gegen eine hochfeste Al-Legierung auszutauschen, um den Wirkungsgrad und die Lebensdauer zu verbessern, allerdings kann dies zu erhöhter Korrosionsgefahr führen.

In diese Arbeit werden zwei verschiedene hochfeste Al-Lotbleche mittels Rasterkraftmikroskopie (AFM) sowie Rasterkelvinsondenkraftmikroskopie (KPFM) untersucht, mit dem Ziel, die physikalischen Parameter zu erkunden, die den Korrosionsprozess beeinflussen. Das Kernmaterial beider Bleche ist  $\text{AlZn}_{4.5}\text{Mg}_1$  und die Lotschicht besteht aus einer eutektischen  $\text{AlSi}_{10}$ -Legierung. Diese beiden Werkstoffe müssen durch eine zusätzliche Zwischenschicht getrennt werden, die eine Diffusion und einen damit einhergehenden Verlust an mechanischer Festigkeit verhindert. Die erste untersuchte Probe hatte eine reine Aluminium-Zwischenschicht (99,85 wt%) und die zweite eine  $\text{AlMn}_1$ -Schicht. Nach einem simulierten Lötprozess (12 min bei  $610 \text{ °C}$ ) wurden metallographische Querschliffe der Bleche für die Untersuchung vorbereitet. Die Untersuchung umfasste die Messung des Lotzustandes mittels AFM und KPFM sowie die topographische Veränderung nach Eintauchen in eine Lösung (42 g/l NaCl, mit Essigsäure auf pH 3 eingestellt) für feste Zeitintervalle von 1 h und 3 h mittels AFM. Mit einer modifizierten Versuchsanordnung war eine KPFM-Messung der  $\text{AlMn}_1$ -Probe nach dem Eintauchtest ebenfalls möglich.

Bei beiden Proben zeigten die Einschlüsse ein edleres Potenzial als die umgebende Al-Matrix.  $\text{Al}(\text{Mn,Fe})\text{Si}$ -Partikel wiesen eine Potenzialdifferenz von ungefähr 300 mV auf. Eindeutige Werte für die Potenzialdifferenzen kleinerer Einschlüsse ( $< 2 \mu\text{m}$ ) konnten nicht ermittelt werden, es ist jedoch eine Tendenz zu höheren Potenzialen erkennbar. Die beiden Proben unterschieden sich durch die Art der Einschlüsse in den Zwischenschichten. In der Probe mit der reinen Aluminium-Zwischenschicht konnte eine hohe Anzahl sehr kleiner Einschlüsse (ca.  $3 \mu\text{m}^2$ ) festgestellt werden.



## Abstract / Kurzfassung

Die Größe und Anzahl dieser Verbindungen nahm mit fortschreitender Korrosion ab. Es war auch möglich, eine Veränderung des Oberflächenpotenzials zwischen den verschiedenen Schichten zu bestimmen. Diese Veränderung war am Rand der Zwischenschicht zum Kernmaterial am ausgeprägtesten ( $1,15 \text{ V}/\mu\text{m}$ ) und ist eine Folge der Diffusionsvorgänge während des Lötens.

Anhand der Ergebnisse der durchgeführten Messungen konnte die Möglichkeit, Korrosionseigenschaften mittels KPFM abzuschätzen, an den untersuchten Proben aufgezeigt werden. Die verwendete Methodik erlaubt den Rückschluss, dass eine AlMn1-Zwischenschicht für hochfeste Al-Lotbleche das geeignetste Material ist, um den Korrosionsangriff unter den hier untersuchten Umständen möglichst gering zu halten. Die Ergebnisse dieser Arbeit legen die Möglichkeit einer weiterführenden Untersuchung über den Effekt der Einschlussgröße auf die Korrosionsbeständigkeit dieser Leichtbau-Materialien nahe.

## Acronyms:

AFM.....	atomic force microscopy
KPFM.....	kelvin probe force microscopy
1xxx alloy.....	Al alloys with at least 99 wt% Al
3xxx alloy.....	Al-Mn and Al-Mn-Mg alloys
4xxx alloy.....	Al-Si alloys
7xxx alloy.....	Al-Zn-Mg and Al-Zn-Mg-Cu alloys
8xxx alloy.....	Al alloys not covered in other series
X800.....	Al-Mn alloy specially developed for brazing sheets
SEM.....	scanning electron microscopy
M.....	metal
M <sup>n+</sup> .....	metal ion
SHE.....	standard hydrogen electrode
E <sub>p</sub> .....	passive potential
E <sub>corr</sub> .....	corrosion potential
BPD.....	band of dense precipitates
V <sub>DC</sub> .....	DC-voltage
CPD.....	contact potential difference between tip and sample surface, also V <sub>CPD</sub> in formulas
Φ.....	work function / surface potential
e.....	elementary charge
ω <sub>AC</sub> .....	AC-voltage frequency / oscillation frequency
δC/δz.....	capacitance gradient
F <sub>el</sub> .....	electrostatic force
F <sub>DC</sub> .....	part of electrostatic force corresponding to V <sub>DC</sub>
F <sub>ω<sub>AC</sub></sub> .....	part of electrostatic force corresponding to sin(ω <sub>AC</sub> t)
F <sub>2ω<sub>AC</sub></sub> .....	part of electrostatic force corresponding to cos(2ω <sub>AC</sub> t)
Δf <sub>0</sub> .....	frequency shift between ω <sub>AC</sub> and measured frequency for KPFM
C <sub>nt</sub> .....	capacitance between sample area n and tip
EDX.....	energy-dispersive x-ray spectroscopy
SWAAT.....	saltwater acetic acid test
RMS roughness.....	root mean square roughness

# Contents

1	Introduction.....	1
2	Theoretical background.....	2
2.1	Aluminum brazing sheets.....	2
2.1.1	Properties of aluminum and chosen aluminum alloys.....	3
2.1.2	Changes during the brazing process.....	5
2.2	Corrosion processes of metals.....	5
2.2.1	Corrosion behavior of aluminium.....	7
2.2.2	Corrosion of Al-brazing sheets.....	9
2.3	Atomic force microscopy.....	10
2.4	Kelvin probe force microscopy.....	12
2.4.1	Amplitude Modulation Kelvin Probe Force Microscopy.....	13
2.5	Influence of the tip geometry -.....	13
2.5.1	- on the topography image.....	13
2.5.2	- on the CPD image.....	14
2.6	Scanning electron microscopy.....	16
3	Experimental.....	18
3.1	Sample preparation.....	18
3.2	AFM and KPFM measurements.....	19
3.3	Data analysis.....	21
4	Results.....	22
4.1	Examination of AlSi10/Al99.85/AlZn4.5Mg1.....	22
4.2	Examination of AlSi10/AlMn1/AlZn4.5Mg1.....	29
5	Discussion.....	40
6	Summary and outlook.....	44
7	Appendix.....	1
7.1	Results for AlSi10/Al99.85/AlZn4.5Mg1.....	1
7.2	Python code to handle the AlMn1 Sample analysis.....	9

# 1 Introduction

Aluminium brazing sheets are used for the construction of automotive heat exchangers and consist of different layers, which fulfill different purposes. The brazing layer has a significantly lower melting temperature than the other used materials, which is around 575 °C compared to 660 °C for pure aluminum. The intermediate layer blocks diffusion from the brazing layer to the base material, while the base material provides the overall strength of the sheet. During the brazing process, the brazing layer melts and flows into the gap between adjacent sheets. During cooling, the liquid solidifies and the joint is formed. At the moment, the most frequently used brazing sheets are utilizing a Al-Mn base material. However, using a high-strength base material instead could lead to an increase of the service life of heat exchangers and improve their performance during service. The aim of this diploma thesis is to characterize different high-strength brazing sheets in regard to inclusions and the variation of the work function between the different layers, employing atomic force microscopy (AFM) techniques. A method, used in this work, to resolve work function variations at the  $\mu\text{m}$ -scale and beyond is kelvin probe force microscopy (KPFM), an AFM variant. Because the life time of heat exchangers is most often limited by its corrosion behavior, the KPFM data is correlated with the corrosion behavior to further improve the understanding of the corrosion process and to emphasize the usefulness of KPFM, for such an investigation.

## 2 Theoretical background

### 2.1 Aluminum brazing sheets

All brazing sheets are multilayered structures, consisting of at least two layers. The base or core material, commonly a 3xxx alloy, clad at least on one side with a lower melting material, usually a 4xxx alloy, which is called the brazing layer in this work [1]. A schematic picture of this layered structure is shown in Figure 2.1 a). This clad melts during the brazing process, when the temperature is kept above the melting point of the clad but below the melting point of the base material. Thus a metallurgical bonding between two adjacent sheets is formed. For heat exchangers with quite complex shapes, brazing sheets are stacked on one another and undergo the brazing process. Between the core material and the brazing layer additional layers can be introduced, e.g. in order to block diffusion from the brazing layer during brazing, a schematic drawing of such a modified sheet can be seen in Figure 2.1 b). Brazing sheets are usually produced by roll-bonding, where the core material is rolled together with the cladding placed on one or both sides of it. The achievable relative layer thickness through roll-bonding is around three to seven percent of the core material. It is important to prevent diffusion between the cladding and the core by choosing the right process parameters during brazing, especially the temperature. If the diffusion is insufficiently inhibited, the strength of the core material is reduced, which can negatively affect the function the final product [2].

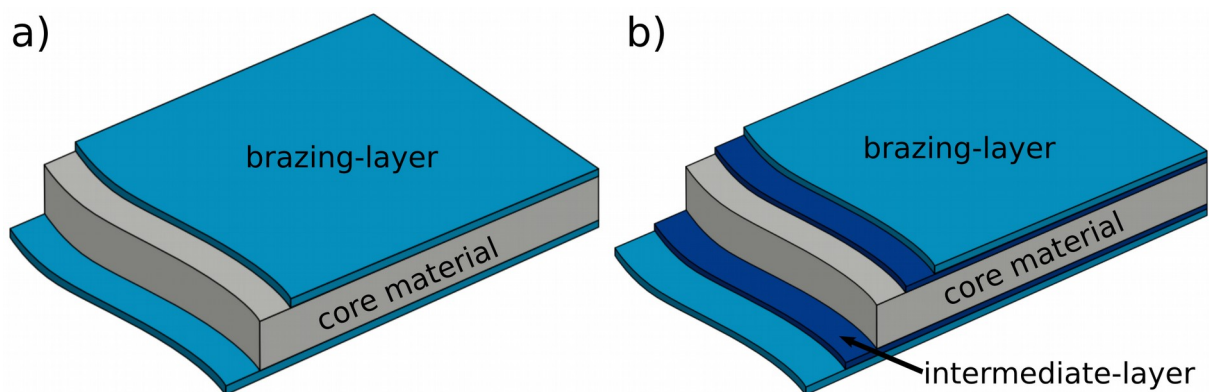


**Figure 2.1:** Systematic sketch of the layered structure of brazing sheets, with a) two layers and b) three layers.

### 2.1.1 Properties of aluminum and chosen aluminum alloys

Aluminum is a good choice for many applications, in which a low density and simultaneously a high electrical or thermal conductivity are required. However, the overall strength of pure aluminum is not sufficient to be directly used for structural parts in most of the applications. Some remedy to this problem can be provided in the form of alloys, but nearly always on the cost of diminishing other properties as a consequence. Therefore, it is (as with every material) important to exactly know the requirements that have to be fulfilled during service.

First, an overview of the properties of pure aluminum, or to be more precise of the 1xxx series consisting of “alloys” with at least 99 wt-% of aluminum will be provided. These alloys have a density of 2.6 to 2.8 g/cm<sup>3</sup> (99.5 wt-%Al has 2.7 g/cm<sup>3</sup>) with a Young’s modulus of 60 to 78 kN/mm<sup>2</sup> (for comparison density of iron 7.85 g/cm<sup>3</sup> with a Young’s modulus of 206 kN/mm<sup>2</sup> [3]) and thermal conductivity from 205 to 232 WK/m. Aluminum crystallizes in a face-centered cubic system [4].

Another important alloy series in this work, the 4xxx series, consists of Al-Si alloys. The main alloying element of this series is silicon, which forms an eutectic system with aluminum. It has a melting point of 577 °C at 12.5 % Si. The two most commonly used representatives of this series are 4032, used for forgings, and 4043, employed as filler material for welding. Most of the 4xxx alloys are used as filler materials in welding or brazing processes, due to their good flow characteristics in the liquid state. The alloys mostly used for brazing-layers are 4342, 4045 and 4047X [5].

The 3xxx series consists of Al-Mn and Al-Mn-Mg alloys. It is used due to the combination of moderate strength, high ductility and good corrosion resistance. Generally, the corrosion resistance of the 3xxx series is comparable to pure aluminum, in some cases even better [6]. By adding magnesium it is possible to raise the tensile strength [7]. The maximum solid solubility of manganese in aluminum is 1.82 %, but because of the possible formation of brittle Al<sub>6</sub>Mn particles which reduces the local ductility, commercial Al-Mn alloys only contain up to 1.25 % manganese. The Al<sub>6</sub>Mn particles form more easily when iron is present in the alloy. Up to 50 % of manganese in the Al<sub>6</sub>Mn particles can be substituted with iron and a mixed phase of Al<sub>6</sub>(Mn,Fe) is formed.

The last series for which a short overview will be provided is the 7xxx series which consists of Al-Zn-Mg alloys and Al-Zn-Mg-Cu alloys. Only the first type of alloy will be addressed. All alloys from the 7xxx series are heat-treatable, and the increase of the strength properties depends on age hardening. Zinc alone as alloying element does not have a strong impact on the strength. Only in combination with magnesium, an



### 2.1.2 Changes during the brazing process

The temperature for the brazing process is chosen between the melting points of the cladding and the other layers (585 – 610 °C). Common claddings melt around 577 °C and form a liquid film. Silicon diffuses into the core, leading to a reduction of the strength through formation of a Al - Si melt, which liquifies around temperatures between 595 °C to 610 °C. Because of the higher diffusion speed at the grain boundaries, melting at these boundaries occurs and can cause a sagging of the construct [8]. High-strength aluminum alloys are more susceptible to this loss of strength. Therefore, a third layer is inserted between core and cladding to prevent the permeation of silicon, when using high-strength alloys. During the heat treatment, the plates undergo a recrystallization and a change of the overall micro-structure. The distinctive interface of the layers, obtained through the rolling process, dissolves and leaves areas with slightly different chemical composition than the surrounding, as shown in Figure 2.3 by scanning electron microscopy (SEM) [9].

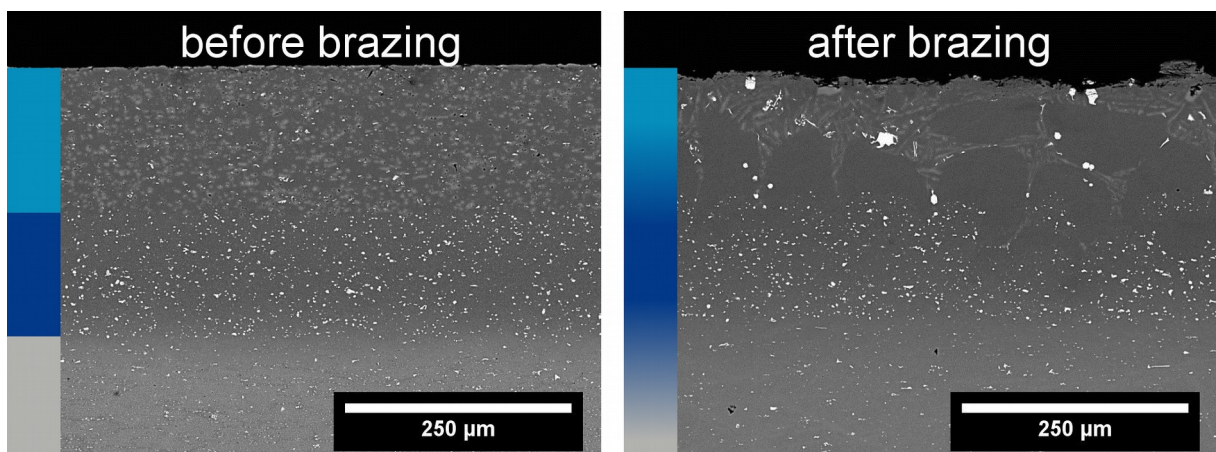


**Figure 2.3:** SEM microscopy of a three-layered brazing sheet, used in this work (AlMn1 intermediate layer), before and after brazing. The change in the structure is most visible in the brazing layer. The layer positions are indicated by the gray and blue bars on the left side of the images. Light blue represents the brazing layer, dark blue the intermediate layer and grey stands for the core material.

## 2.2 Corrosion processes of metals

Corrosion is defined as the destruction or degradation of a metal in reaction with its environment. It can be categorized in some cases into physical and chemical corrosion. Physical corrosion involves wear from dust, or from other particles in a moving medium, but this will not be discussed in this work. For brazing sheets, the chemical corrosion is of greater importance. Only this kind will be described. The



chemical corrosion can be broken down into two parts. The first partial reaction is the oxidation or dissolution of the metal according to equation 2.1. This reaction is equivalent to an anodic reaction in a galvanic cell [10].



Not only this anodic reaction is necessary, but also a cathodic reaction, which provides the necessary electrons and sustains the reaction. Equation 2.2 shows the typical cathodic reaction in acidic environments and solutions (hydrogen evolution reaction) and also the reaction corresponding to the standard hydrogen electrode (SHE).



Not only hydrogen can be reduced, but also other metal ions can be used in the cathodic reaction, as well as oxygen consumption in an alkaline solution. Because the cathodic and anodic reactions are accompanied by an electron transfer, it is possible to influence them via an electrical potential and protect against or increase corrosion. Also the accumulation of ions near the surface can alter the corrosion process. Further the diffusion and availability of the reactants are of great importance. With this in mind, it is clear that the corrosion dynamics are not simple at all and are influenced by temperature, electron charge, movement of the fluid, and other parameters [11].

Because most corrosion processes involve water, a possibility to describe the reactivity of a metal is to compare it against a reference electrode in a galvanic cell and measure the potential difference. These setups are calibrated against the standard hydrogen electrode (SHE), which is arbitrary set to 0 V, so that the measured potential is equivalent to the half cell potential of the metal. Usually, the measurement is not done against SHE but other reference electrodes (most common: calomel electrode), due to the complicated setup of the SHE. Ordering the metals according to the half cell potential, leads to the Standard Electromotive Force potential series, with the noble materials on the top and the active metals on the bottom (see Table 2.1). If a noble material is in contact with an active material and an electrolyte is present, it is possible to predict that the active metal will start to corrode. It must be noted that the order of the electromotive force table will vary, depending on the used electrolyte. An important behavior of some metals in a corroding environment is the so called passivity, and this refers to the decline of the corrosion rate above a certain potential  $E_p$ . The reason for this reduction is a thin, protective layer build out of hydrated oxides, or other corrosion products [11].

## 2.2.1 Corrossion behavior of aluminium

As it can be seen in table 2.1, aluminium has with -1.66 V vs SHE a more negative electromotive force than iron (-0.44 V vs SHE). However, it is known to be more resistant to corrosion.

**Table 2.1:** Excerpt of the Standard Electromotive Force Potentials [11].

Reaction	Standard Potential, $e^\circ$ (volts vs. SHE)
$\text{Au}^{3+} + 3e^- = \text{Au}$	+1.498
$\text{Pt}^{2+} + 2e^- = \text{Pt}$	+1.118
$\text{Ag}^+ + e^- = \text{Ag}$	+0.799
$\text{Cu}^{2+} + 2e^- = \text{Cu}$	+0.342
$2\text{H}^+ + 2e^- = \text{H}_2$	0
$\text{Fe}^{2+} + 2e^- = \text{Fe}$	-0.447
$\text{Zn}^{2+} + 2e^- = \text{Zn}$	-0.762
$\text{Al}^{3+} + 3e^- = \text{Al}$	-1.662
$\text{Mg}^{2+} + 2e^- = \text{Mg}$	-2.372

The reason for this perceived higher stability is a protective and stable oxide layer on the aluminium surface. This small oxide layer (5 nm in air, thicker at higher temperatures or in water) forms fast and exhibits self-repairing properties in most environments. It consists of a thin compact amorphous barrier layer on the metal and a porous hydrated oxide on top of the barrier layer. The formation of the porous layer can be considered as a local impairment of the barrier layer and a reoxidation of the metal below. In case that the environment is not damaging the oxide layer, solely the barrier layer exists. If the barrier layer is not stable enough in certain environments, it is possible to oxidate the whole metal block. Something similar is used for the production of fine aluminium oxide filters used in the field of chemistry [11],[12].

Aluminium is passive in a pH-range between 4 to 8.5. Beyond this range the oxide layer can be soluble with the suitable acids or bases. Most metallic corrosion processes are in some form electrochemical in nature, and because of that the solution potential (or corrosion potential  $E_{\text{corr}}$ ) is important for understanding the corrosion process. If the solution potential of two electrochemically different parts or areas is different enough they show a inclination to form a galvanic couple and

therefore, the anodic area will electrochemically corrode. The potential of the metal matrix can be influenced through different alloying elements, whereas the composition of the common inclusions (intermetallic compounds) only vary in small windows as well as their solution potential. Besides the difference in the potential of the constituents is pertinent for the corrosion behavior, also the ratio and distribution is important.

Galvanic corrosion is the accelerated dissolution of the more reactive metal in "contact" with a more noble material in a conductive environment (electrolyte). This mechanism does not have a distinctive form of attack itself, but it accelerates the other forms of corrosion (e.g. pitting). The two materials don't need to be in direct physical contact with each other, it is sufficient to be linked via a conductive material. Because of different chemical reactions, the order of reactivity, and predominant attack type has to be determined for each conductive environment separately. In the pH range of 4.5 to 9.0 (where the oxide film is stable), the most common corrosion mechanism is in the form of pitting. Pitting corrosion is most often the result of different airing of the surface and a resulting change in the corrosion potential at the bottom of the pit. The starting points are usually defects within the oxide layer. The corrosion rate is fast in the beginning, and diminishes due to the required mass transport to the corroding site. The pitting resistance is directly connected to the purity of the alloy. Usually it can be observed that the 1xxx series exhibits a slightly higher resistance to pitting than the 3xxx alloys, which have a higher resistance than the 7xxx alloys. The small change in resistance between the pure aluminium and the 3003 alloy is explainable by the electrochemical potential of the AlMn particles in those alloys, which is nearly the same as the electrochemical potential of aluminium itself. Because of the low pitting resistance of the 7xxx alloys they are clad. It can be stated that a lower copper content yields a higher pitting resistance. Thus the copper free alloys are better suited for pitting environments [7].

Also, a common corrosion appearance is intergranular corrosion, which shows as a corrosion along the grain boundaries and yet intact grains. This can occur in combination with precipitations of secondary phases. The formation of these phases can leave an area in the matrix depleted of some alloying elements. Because of this depletion, a corrosion potential drop between this area and the undepleted grain is present, which can lead to a galvanic reaction as well as the corrosion potential difference between the secondary phase and the matrix. Intergranular corrosion is common in the 2xxx and the 7xxx series. In both of them mostly on alloys with copper as an alloying element. In highly elongated microstructures, such as rolled sheets, a preferred longitudinal propagation direction is possible, which can lead to

exfoliation. This is a type of intergranular corrosion, where the grains don't fall out. However, because of the resulting stress because of the higher volume from the corrosion products leads to a laminated attack [7].

### **2.2.2 Corrosion of Al-brazing sheets**

For heat exchangers, a critical failure mode is the penetration of the wall separating the hot and cold channels. Therefore pitting corrosion is considered as a severe problem, and the corrosion behavior of the used alloys as well as the sheets in the brazed state are constantly under study. To understand the processes during corrosion, it is necessary to explore the influence of inclusions and their role in the corrosion process. In [13] it is shown that inclusions containing Fe, Cu, and/or Ti (as example:  $\text{Al}_3\text{Fe}$ ,  $\text{Al}_7\text{Cu}_2\text{Fe}$ ) are more noble than Al. This leads to a dissolution of the matrix material around these inclusions. The inclusion acts as the cathodic part in this corrosion process. Mg, Zn, Si containing inclusions (as example:  $\text{Mg}_2\text{Si}$ ,  $\text{MgZn}_2$ ) are less noble than Al and will dissolve preferentially in a corroding environment. Both behaviors can lead to damage like surface cavities, which can be the starting places for pitting, exfoliation or intergranular corrosion. An interesting fact is that not only the  $E_{\text{corr}}$  is of importance, but also the current present during the corrosion to understand the corrosion kinetics. A high current could result in a faster reaction speed, which leads ultimately to a higher corrosion rate and a faster failure. On some inclusions ( $\text{Al}_2\text{CuMg}$  for an example) it can be assumed that a dealloying mechanism takes place and that the corrosion potential changes during the corrosion [14].

Intergranular and exfoliation corrosion are the main types of corrosion attack in classical aluminium brazing sheets. Because the penetration through the sheet would lead to a premature failure, a way to steer the direction of the corrosion was found. Through elongation of the grains, it is possible to direct the intergranular corrosion somewhat into the orientation of the sheet. In some brazing sheets (for example a combination of a X800 core with AA4104 cladding), a band of dense precipitates (BPD) exists near the border area of the cladding to the core. This BPD consists of inclusions with a size of 20-50  $\mu\text{m}$  and also steers the corrosion attack into the less significant direction of the sheet. Thus, it promotes delamination in the sheet. Such a slow delamination in this direction is a lifetime gain for the heat exchanger compared to a breach, which immediately leads to failure [14],[15].

## 2.3 Atomic force microscopy

Atomic force microscopy (AFM) is a standard method used for imaging the topography on the nanometer scale. Topography is acquired by scanning a sharp tip-like probe across the sample surface. The AFM probe can be imagined as a small tip (tip radius in the case of this work is about 35 nm) attached to the free end of a  $\mu\text{m}$ -size cantilever. Figure 2.4 shows an SEM image of the free cantilever end with the pyramid shaped tip.

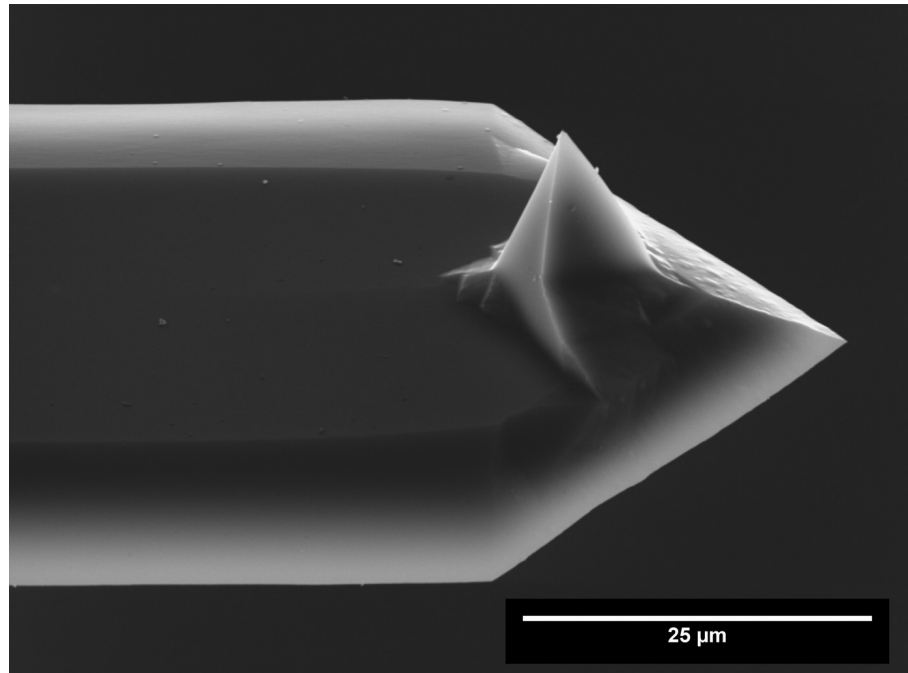


**Figure 2.4:** SEM image of a probe used in this work. (Recorded by Dr. Thomas Kremmer.) The tip was slightly dulled in the process of the measurement.

To obtain values for the height differences on the sample surface, the deflection of the cantilever is measured, most commonly done with a laser reflected from the backside of the cantilever to a position sensitive photodetector. This photodetector is a split photodiode and consists of four different segments. It allows to measure vertical deflection as well as torsion of the cantilever simultaneously [16]. For the deflection, the signal difference between the upper and lower half of the photodiode is used; a schematic representation of this method is presented in Figure 2.5. The movement of the tip with regard to the sample surface in lateral directions ( $x$  and  $y$  direction) as well as controlling the tip - sample distance ( $z$  direction), is accomplished with the use of piezoelectric actuators. AFM can be used in different modes: contact-, non-contact-, and intermittent contact mode (tapping mode).

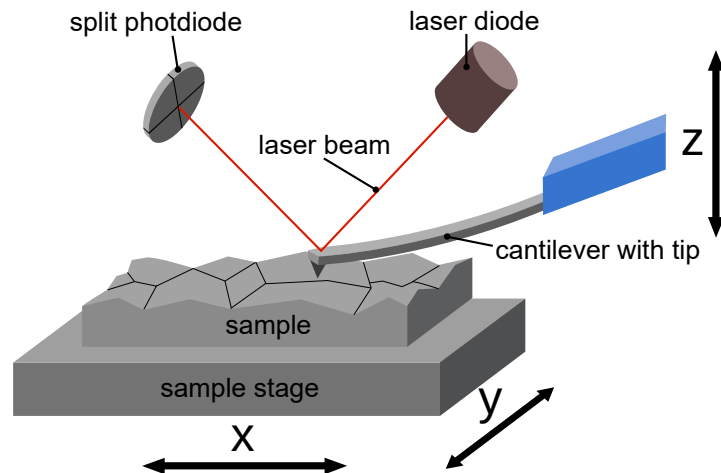


**Figure 2.5:** Operating principle of the laser deflection readout method for AFM. Movement in x and y direction is realized through piezoelectrically induced movement of the sample stage and z-direction through movement of the cantilever holder.

In contact mode, the tip is brought into contact with the surface and scans across it, line by line. This mode is straight forward to understand but has some drawbacks, e.g., the strong interaction with the surface, which can lead to significant changes in the topography or tip shape and in extreme cases a destruction of tip and/or surface. The height can be gathered in two different ways, by keeping the deflection constant and using the signal of the piezo used to adjust the z-distance or by keeping the height constant and using the deflection as described before.

The second mode, non-contact mode, is harder to understand. In this mode, the cantilever is excited to vibrate near its resonance frequency at low amplitude (~1 to 100 nm) and positioned near the surface, but not touching it. Even though the tip is not in contact with the surface, there is an attractive tip-surface interaction that alters the cantilever oscillation. The frequency of the oscillation gets shifted, due to the change in interaction, if the distance between the tip and the surface alters. A feedback activates the z-piezo such that the tip-sample distance and hence the frequency shift stays constant. The necessary z-piezo movement then contains the height information [17]. This frequency modulation technique is most often used in high vacuum or ultra-high vacuum.

Intermittent contact mode (frequently also called tapping mode), is an intermediate between contact and non-contact mode. The cantilever is brought to vibration near the resonance frequency by piezoelectric elements and is approached close enough to the surface to periodically tap (come into repulsive interaction regime) the sample surface. Height information is gathered by monitoring the change in z - direction necessary to keep either the amplitude (AM - mode) or the frequency (FM - mode)

constant. It is also possible to measure the phase shift between the exciting oscillation and the actual oscillation of the cantilever [18]. In this way information about adhesive, mechanical, and dissipative properties can be obtained [19],[20]. Some interaction with the surface is still occurring, but much less than in contact mode, and there is no need to measure in vacuum. Tapping mode is the most frequently used mode for topography measurements under ambient conditions.

## 2.4 Kelvin probe force microscopy

Kelvin Probe Force Microscopy (KPFM) is an AFM based method to measure the local surface potential or the work function of materials. The principle behind this method is comparable to the macroscopic Kelvin probe technique, in which one of the two plates of a parallel plate capacitor is brought to vibration. The change of the capacitance leads to an alternating current in the circuit connecting these plates. This current is nullified by applying a DC voltage ( $V_{DC}$ ) to one plate. The dc voltage for which the current is zero corresponds to the contact potential difference (CPD), which can be considered as the difference in the work function ( $\Phi$ ), between the plates.

$$V_{CPD} = \frac{\Delta\Phi}{e} = \frac{\Phi_{plate\ 1} - \Phi_{plate\ 2}}{e} \quad (2.3)$$

$e$  in this equation stands for the elementary charge. Now, we consider the sample as plate 1 and the tip as plate 2 of the capacitor to see the analogy. The difference, besides the nanometer resolution, is, while the Kelvin Probe technique uses the DC-voltage as controlling parameter, KPFM uses the electrostatic force, because the cantilever is in its nature very sensitive to changes of forces. The vibration of the cantilever is not mechanically induced, but through applying an AC voltage with a frequency  $\omega_{AC}$ , which leads to an oscillating electrostatic force responsible for the oscillation of the cantilever with  $\omega_{AC}$ . The resulting electrostatic force can be expressed as

$$F_{el} = -\frac{1}{2} \frac{\delta C}{\delta z} [V_{DC} - V_{CPD} + V_{AC} \sin(\omega_{AC} t)]^2 \quad (2.4)$$

Whereas  $\delta C/\delta z$  is the capacitance gradient of the tip sample system (with respect to the tip-sample distance),  $V_{DC}$  the compensating dc voltage,  $V_{CPD}$  the contact potential difference of the sample tip system (with the sample as plate 1 and tip as plate 2, because of the algebraic sign) and  $V_{AC} \sin(\omega_{AC} t)$  the AC voltage used for the cantilever oscillation. This equation can also be written as

$$F_{el} = F_{DC} + F_{\omega_{AC}} + F_{2\omega_{AC}} \quad (2.5)$$

with

$$F_{DC} = -\frac{\delta C}{\delta Z} \left[ \frac{1}{2} (V_{DC} - V_{CPD})^2 + \frac{V_{AC}^2}{4} \right] , \quad (2.6)$$

$$F_{\omega_{AC}} = -\frac{\delta C}{\delta Z} (V_{DC} - V_{CPD}) V_{AC} \sin(\omega_{AC} t) , \quad (2.7)$$

$$F_{2\omega_{AC}} = -\frac{\delta C}{\delta Z} \frac{V_{AC}^2}{4} \cos(2\omega_{AC} t) . \quad (2.8)$$

For a non-contact measurement the  $F_{DC}$  part would contribute to the topography image and the term  $F_{2\omega_{AC}}$  can be used for capacitance microscopy. Two modes can be employed for the CPD measurements. The amplitude modulation technique where the amplitude of the oscillation at  $\omega_{AC}$  is brought to zero with  $V_{DC}$  and the frequency modulation technique which minimizes the frequency shift  $\Delta f_0$  at  $\omega_{AC}$  [21]. Only the amplitude modulation technique will be described and applied in this thesis.

### 2.4.1 Amplitude Modulation Kelvin Probe Force Microscopy

By Amplitude Modulation Kelvin Probe Force Microscopy (AM-KPFM) the CPD is measured by minimizing the amplitude, which is proportional to the induced electrostatic force, by tuning  $V_{DC}$  to  $V_{CPD}$  (see (2.5)). The amplitude of the cantilever oscillation is detected via the beam deflection signal and a lock-in amplifier tuned to  $\omega_{AC}$ . Often, AM-KPFM is accomplished as a two-pass mode, where the first pass is used to scan the topography and the second pass to measure the CPD. In the second pass, the tip is raised some nm to some ten nm above the surface of the sample and moved along the already measured topography at a constant height. The oscillation frequency  $\omega_{AC}$  is tuned close to the resonance frequency of the cantilever, to lower the AC-voltage and to increase the sensitivity to the electrostatic force. It should be mentioned that it is possible to measure the topography and the CPD in one scan, if the mechanical excitation for the tapping mode is tuned to the first oscillation mode of the cantilever and the AC voltage used for the CPD determination to the second oscillation mode, but this technique was not used in this work [22].

## 2.5 Influence of the tip geometry -

### 2.5.1 - on the topography image

The tip geometry has a big impact on the resolution and overall imaging quality. A fine, sharp tip provides the best topography images. The reason for this is simple: the lateral resolution is directly depending on the tip curvature radius and the cone angle. A bigger radius and/or angle leads to a lower resolution, because the cantilever will react to the surface features as soon as some part of the tip is in contact, or close



enough to be influenced. Thus, the features will be imaged broader in the case of hills or smaller in case of holes than they really are. It is also important to understand that if the surface structure is smaller/sharper than the tip, not the feature will be imaged but the tip itself, this phenomenon called tip dilation is sometimes used for tip characterization [22].

After some scans with contact to the surface, the tip can wear and become dull, which brings us to the next problem. If the tip is broken, there will be most likely a rough undefined fractured surface, which can have more than one tip. This can lead to false images in regard to diameters and surface characteristics, such as a multiple detection of a surface hill. A schematic illustration of these artifacts is presented in Figure 2.6. The lateral offset, shown in Figure 2.6, is only a problem when the tip breaks during the ongoing scan. Because only a difference in the offset between areas scanned before the incident and areas scanned after it, will have an impact on the measured surface geometry. The bigger problem is the multiple registrations of surface geometry objects, also called ghost images, because of multiple "tips" on the fractured tip surface.

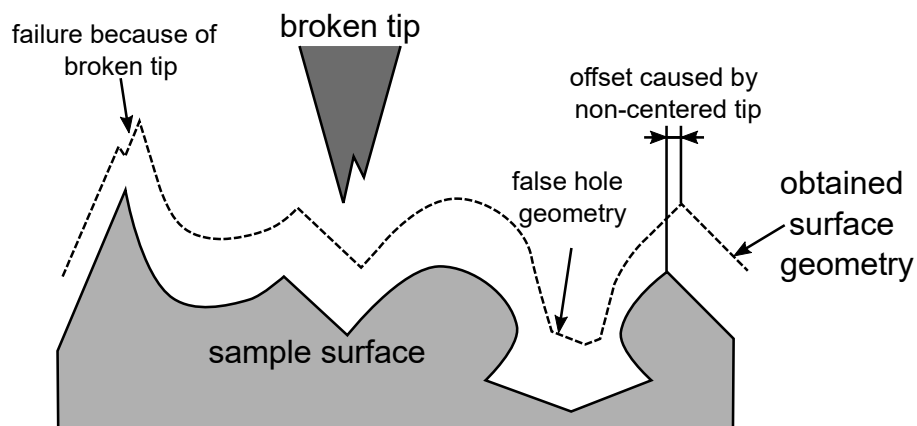


**Figure 2.6:** Scheme of the imaging artifacts, caused by the geometry of the tip.

### 2.5.2 - on the CPD image

The tip influence on the CPD measurement is harder to explain because of the long range nature of the electrostatic force. Not only the tip/sample capacitance is involved, but also the capacitance between the cantilever/sample and surface of the cone and sample are involved, as is illustrated in Figure 2.7.

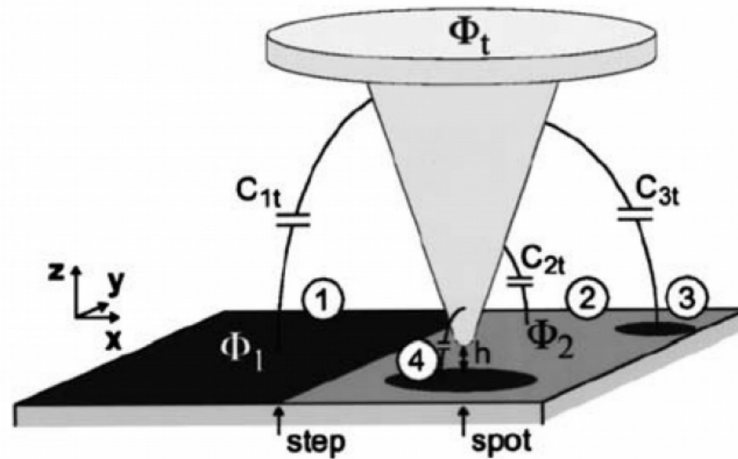


**Figure 2.7:** Schematic of the capacitances ( $C_{1t}$  to  $C_{4t}$ ) influencing the measurement, because of different local surface potentials  $\Phi_1$  to  $\Phi_2$ . Adapted from [23]. 1, 3 and 4 shows the effect from surfaces with the potential  $\Phi_1$ . 1 is to the mantle of the tip, from a bigger surface, 3 is the same from some small inclusion, and 4 is the interaction of the spot, to the tip, and mantle. 2 is representative for the interaction of the surface area with potential  $\Phi_2$  to the tip mantle.

Many models were created, to understand the influence of the tip geometry on the measured CPD. One of the rather simple models represents the tip as concatenation of parallel plate capacitors, forming a pyramid as presented in Figure 2.8 (together with schematic drawings of other models) [24]. This model has two major weak points. First, it underestimates the area under the tip, and second the parallel plate capacitor assumption is only valid for a small gap between the plates with respect to their area, which is not fulfilled for a realistic representation of a cantilever and the tip. Also, the cantilever itself is not considered. Other simulations for the interactions were made by modeling the tip as a sphere on a cone [25] or a cone, on a triangular cantilever, ending in a hemisphere [26]. These models help to understand that not only the tip and the surface under the tip are contributing to the signal. Additionally, the tip radius and the probe-sample separation are extremely important for the lateral resolution for small separation heights  $< 10$  nm. For higher separation heights, the force on the cantilever prevails, because of the area difference between tip (small) and cantilever (big). This can be modified through tip radius (tuning the effective area ratio between cantilever and tip), tip height (increasing the distance from the sample to the cantilever) and bigger cone angles. All three possibilities decrease the effect of the cantilever surface and increase the dominance of the interaction between tip and sample. Resulting in the measured force to be mainly caused by the tip interaction. One problem (also important for the topography imaging, but to a lesser degree) is

that during the measurement the tip can get contaminated and thus the workfunction will undergo changes. Then, the gathered signal is the CPD between the sample and the contaminant together with the tip, shaft, and cantilever. In the worst case, the image becomes useless, because the gathered value is not comparable to other measurements. In the best case there will be just a minor constant jump in the gathered CPD values, which can be corrected. However, such results cannot be trusted completely and therefore cannot be analyzed quantitatively.

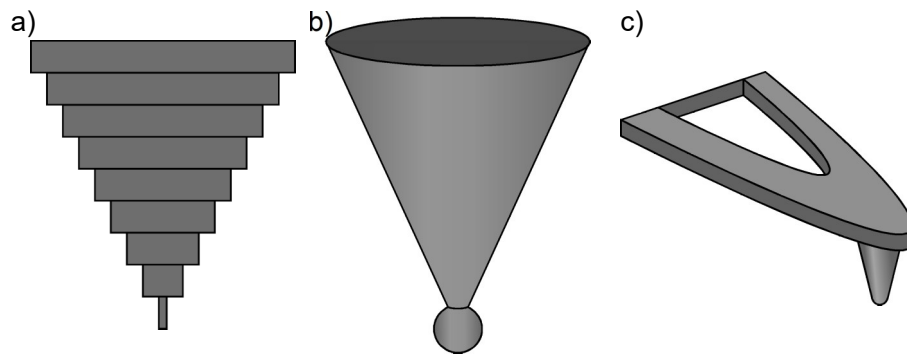


**Figure 2.8:** Schematic drawings of modeled probes. a) square plate capacitors, stacked to form a pyramid; b) cone with a sphere at the end; c) triangular cantilever with cone tip, ending in a hemisphere. Drawing of the models described in [25] (a), [26] (b) and [27] (c).

## 2.6 Scanning electron microscopy

Scanning electron microscopy (SEM) is a powerful tool for high resolution imaging as well as sample characterization. Analogue to AFM, a line-by-line scan is performed on the sample, but with an focused electron beam instead of a tip. The obtainable resolution is directly dependent on the beam diameter and the interaction volume, which are dependent on the acceleration voltage and the electron source. The different electron sources, as well as detectors will not be described in this work. They are described in [27]. SEM is comparable with classical light microscopy in regard to the beam path. The “lenses” to control and focus the electron beam use either electrostatic or magnetic fields to deflect the electrons.

The beam interacts with the material through elastic and inelastic scattering, and the results are electrons with different energies and characteristic x-rays as well as Bremsstrahlung. One important fact in understanding the results of SEM is that the interaction is not only restricted to the surface, but there is also a volume contribution as indicated in Figure 2.9.

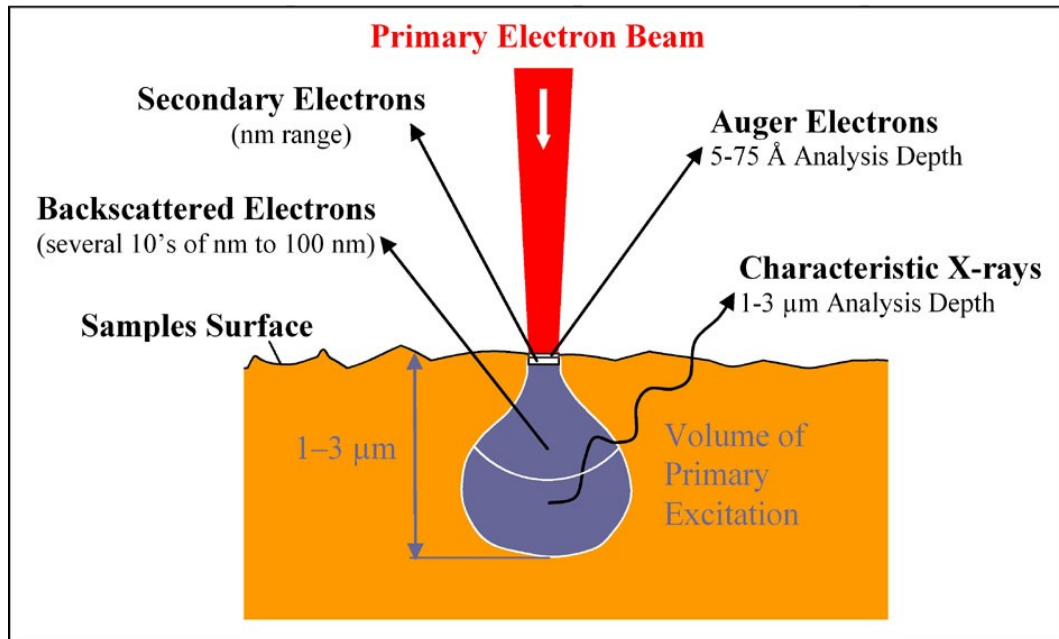


**Figure 2.9:** Schematic drawing of the interaction volume, which shows the different measurable interactions between the primary electron beam and the sample. Picture is used from [28].

The size of the interaction volume is dependent on the used acceleration voltage and the atomic number of the sample material (to a higher atomic number there is a smaller excitation bulb) and can reach several  $\mu\text{m}$  depth [28]. The different electrons created by the interaction between the primary electron beam and the sample can be classified by the process which leads to their emission. For imaging, mostly secondary electrons and backscattered electrons are used. Secondary electrons are the result of many inelastic scattering processes and have a small kinetic energy ( $< 50 \text{ eV}$ ), which is the reason why they can only leave the sample when emitted near the surface (1-10 nm). This kind of resulting electrons is most commonly used for imaging of the surface (topography). Another way to generate an image of the sample, is to use the elastically back scattered electrons with a medium to high kinetic energy. Elements with a higher atomic number cause more back scattered electrons. The topography influence is higher than with secondary electrons. To gather more information of the sample, the resulting x-rays can be used. The resulting x-rays can be differentiated into x-ray bremsstrahlung and characteristic x-rays. The characteristic x-rays which are emitted when an outer shell electron jumps into an energetically lower vacancy are specific to the atoms of their origin and can be used for chemical characterization. This analysis technique is called energy-dispersive x-ray spectroscopy (EDX). The vacancy is a result of the ionization caused by electron collision from the primary electron beam [28].

## 3 Experimental

### 3.1 Sample preparation

Two sheets cladded on both sides, both consisting of AlZn4.5Mg1 as the core material and AlSi10 as the brazing layer and an intermediate layer, in one case Al99.85 and in the other one AlMn1, were examined. These samples were provided by AMAG rolling GmbH (Ranshofen, Austria). The layer thickness of the intermediate and brazing layer were both around 140  $\mu\text{m}$ . The overall thickness of the sheets was 1.5 mm. The samples will further be referred to by the name of the used intermediate layer, because the core material and brazing layer were the same. These sheets were cut into 50 mm to 70 mm wide pieces for better handling and put into a convection oven for a simulated brazing process, at 610 °C for 12 min (Figure 3.1 b).

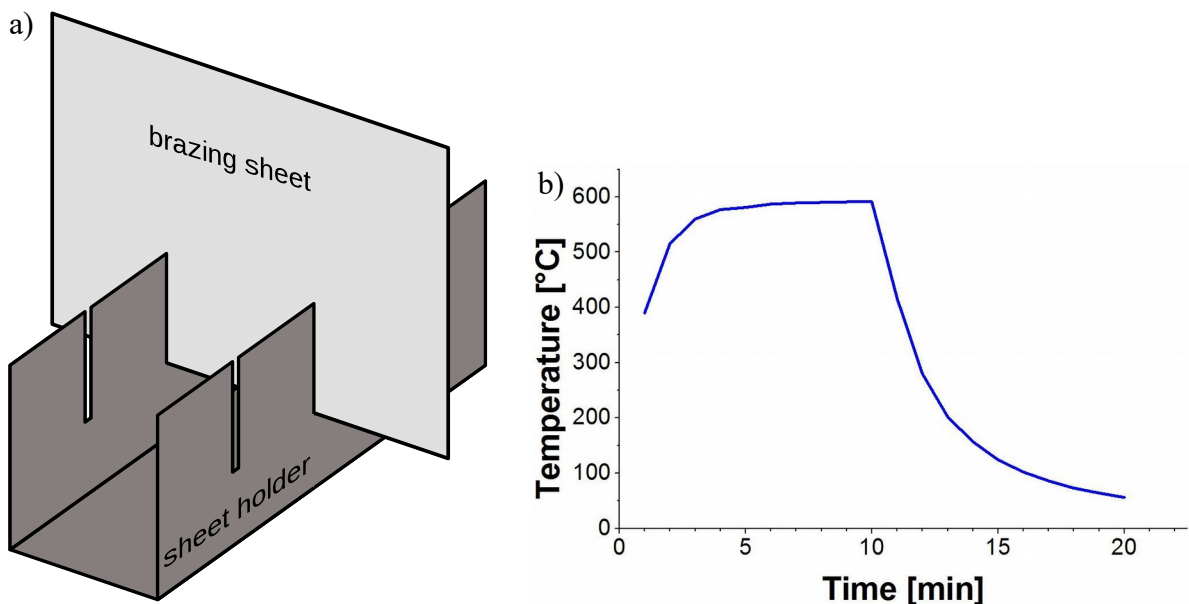


**Figure 3.1:** a) Schematic drawing of the used sheet holder (not to scale) and b) Temperature-Time profile of the brazing cycle.

For a more uniform heat treatment, a special holder with an U-shaped profile was used. It was fabricated from a rectangular tube where one wall was cut away. Small slices to take up the sheets were cut into the remaining walls (Figure 3.1 a). With this holder, the sheets were standing almost free in the oven, and only small areas could not be used for investigation, namely the area in direct contact with the holder and the outmost areas of the sheet. The outmost areas couldn't be used, because the liquid melt of the brazing process would pool together at the bottom of the sheet, whereas it would flow away at the top, and on the corners it would migrate along the corner. After the brazing cycle, small samples (6 mm to 15 mm) were taken out of the

middle of the sheets and embedded in a resin for cold mounting. After the hardening of the resin, the samples were polished on one side up to a polishing agent of 0.1  $\mu\text{m}$  and cleaned in an ultrasonic bath filled with isopropanol. By optical microscopy, the surface was controlled for scratches, which could disturb measurements. Interesting areas of the sample (core material, intermediate layer, and the border between these two) were selected for further investigation. In Figure 3.2 the areas of interest are marked by squares.

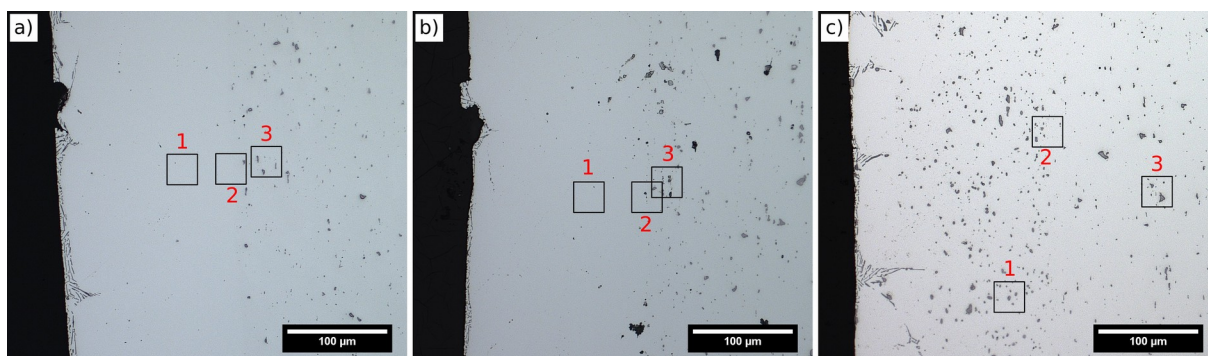


**Figure 3.2:** Light microscopy images of the three samples investigated. a) Al99.85 used for the KPFM analysis. b) Al99.85 used for the analysis of the corrosion process. c) AlMn1 used for both KPFM and corrosion process analysis. The three squares in each image are from left to right: (1) the intermediate layer-, (2) the border-, and (3) the core material area used.

### 3.2 AFM and KPFM measurements

30 x 30  $\mu\text{m}^2$  areas of the regions of interest were selected for investigations by atomic force microscopy and Kelvin probe force microscopy. The 30  $\mu\text{m}$  x 30  $\mu\text{m}$  measurements were carried out using an Asylum MFP 3D device with a closed-loop scanner. NSG30/TiN conductive probes from NT-MDT were used. They have a tip height of 14 to 16  $\mu\text{m}$ , a tip radius of curvature of 35 nm and a 20 - 30  $\mu\text{m}$  thick TiN coating. The cantilever spring constant was typically 42 N/m and the resonance frequency was between 260 kHz and 300kHz. The samples had to be electrically grounded for the KPFM measurement. This was accomplished with Ag contact paste to form a conducting connection from the metallic sample to a wire which connected it to the metallic frame of the AFM system. In the case of the Al99.85 sample, the paste was applied on top of the polished surface, whereas the AlMn1 sample was connected from the backside, which can be seen in Figure 3.3.

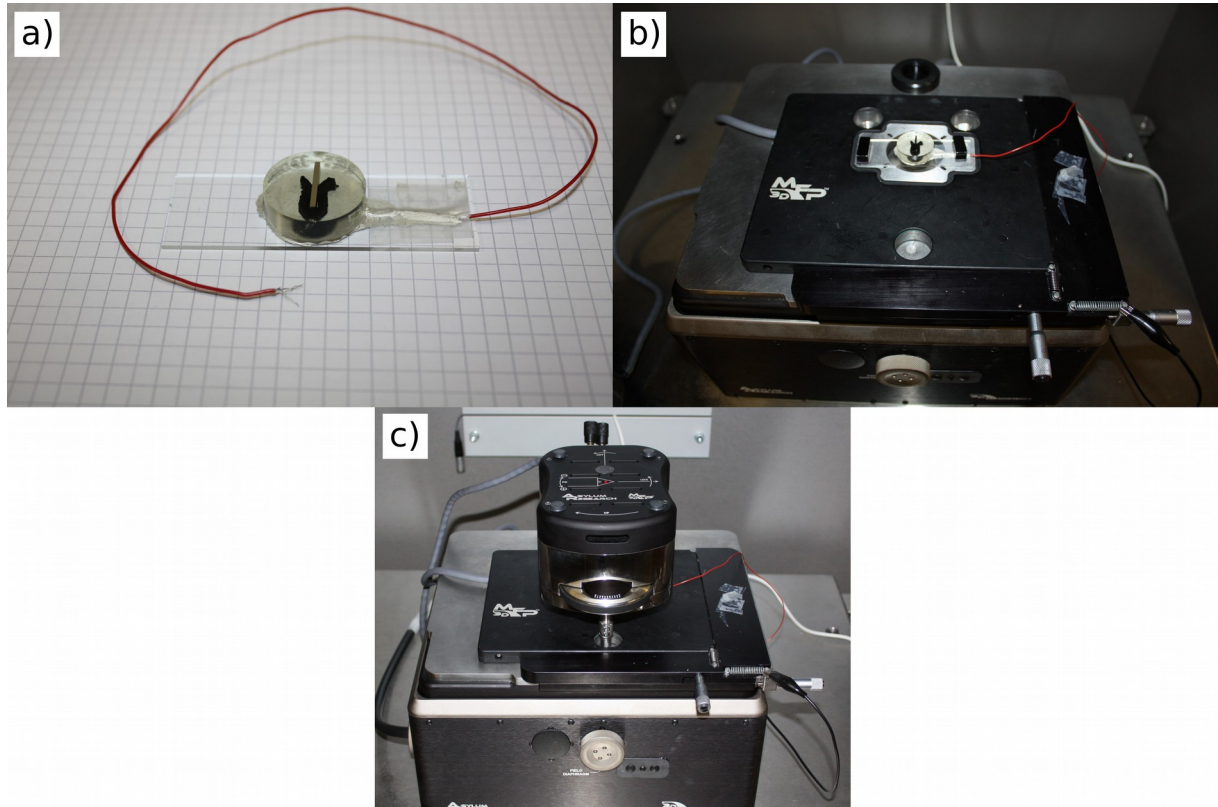


**Figure 3.3:** Sample preparation for the AFM/KPFM measurements. a) Fixing the AlMn1 sample on a specimen holder and establishing a connection to the wire with the contact paste. b) Positioning the sample on the scanner and connecting the wire to the frame. c) Placing the AFM – head over the sample.

Scanning speed for the measurements was chosen to be  $6.8 \mu\text{m/s}$  with a resolution of  $512 \times 512$  pixels, which yielded a measuring time of 2.5 h per frame, for the KPFM analysis, and 1.25 h for topography only measurements. The longer measurement time for KPFM is because each line has to be scanned twice. In the first scan, the topography is obtained, for the second scan the cantilever is lifted by 20 nm to obtain the CPD values. In [29] a similar analysis was done on an AA2024-T3 Al-alloy, with step heights from 50 to 300 nm with no effect on the measured potential. But because of the experiments presented in [24] a smaller tip/sample separation was selected. Both, trace and retrace images were recorded for quality checking.

After this first series of measurements, the samples were subjected to an immersion test with a modified SWAAT solution. SWAAT refers to a corrosion testing after ASTM G85 annex A3 (saltwater acetic acid test, cyclic) in which a sample is introduced to an indirect spray of synthetic sea water and higher temperatures, to emulate different climates and exposure to sea water [30]. Here, the sample was put into a corrosive medium for a fixed time at room temperature, and the changes of the topography

were evaluated afterwards. The SWAAT solution was composed of 42 g/l NaCl dissolved in H<sub>2</sub>O and brought to pH 3 with acetic acid (CH<sub>3</sub>COOH). The changes were investigated after 1 h, 3 h, and in the case of the AIMn1 sample for 9 h. For the sample with the Al99.85 intermediate layer, a different sample than for the first measurement was used for corrosion testing, in order to avoid that contact paste necessary for the KPFM measurement contaminates the solution. This problem was solved for the sample with the AIMn1 intermediate layer, through polishing both sides until a contact could be established on the backside and hanging it face down into the solution. In contrast, the Al99.85 sample was put at the bottom of the glass face up. Thus, it was possible to measure also the changes of the CPD signal caused by ongoing corrosion on the AIMn1 sample. After the corrosion time intervals, the sample was once more cleaned in an ultrasonic bath filled with isopropanol and the changes were measured by AFM.

### **3.3 Data analysis**

Most of the data evaluation was performed with Gwyddion, a free and open source software for scanning probe microscopy data visualization and analysis [31]. Generally, the first step was to level the topographic image with the “Plane Level” function provided by the software, which is the subtraction of an average plane constructed from all image points of the data. If bigger signal jumps between individual scanning lines were observed, one of the “Align Rows” commands was also applied, in which the median of each line was subtracted from the line and with this the lines were all set to the same level. After the leveling, the minimum value of the image was set to zero, by the “Fix Zero” command and profiles of the interesting sections were extracted with the “Profile Extraction” tool or marked with a mask, and the values under the mask were analyzed.

For the analysis of the KPFM images, the “leveling” and “align rows” commands were not used, to avoid data bias. Two kinds of values can be obtained from the KPFM images, CPD refers to the contact potential difference between the tip and the surface features on the sample, and the second one will be called “CPD-difference” and is used to compare the CPD of two surface features.



## 4 Results

### 4.1 Examination of AlSi10/Al99.85/AlZn4.5Mg1

In the AFM images (Figure 4.1 – 4.3), three different features can be distinguished: bigger inclusions in the core material area (most likely AlFeSi, see appendix), little inclusions, called dispersoids and the Al - matrix, which refers to the alloy material in which the inclusions are embedded, with changing composition compliant with the area under observation. The most interesting features of this sample are the little inclusions (with a mean diameter of around 500 nm, where the biggest have a diameter up to 3  $\mu\text{m}$ ), so the examination of this sample is focused on their analysis. To obtain statistical data of these inclusions, a mask was placed on the image via the “Mark by Threshold” tool, where the slope was used as threshold parameter with a value between 4 % and 6 %. This way, the little inclusions could be isolated for evaluation. Using the variation of the slopes was necessary, to compensate for topographical differences of the areas and in some cases to exclude corrosion residues. The resulting mask was modified with the “Mask > Morphological Operation” through which little holes, left in the mask through the automatic procedure, were closed with the operation “Closing”. As structural element for this closing procedure, a disc with a radius of 1 pixel was chosen. After this, the mask was altered with the “Mask Editor” and “erase continuous parts of mask” drawing tool, to manually remove those parts of the mask which were set erroneously by the automatic marking procedure. The product of this masking sequence for the investigated area of the intermediate layer is exemplarily illustrated in Figure 4.1 where the masked generated on the topography image (Figure 4.1 a) is seen in c. In d, this mask was overlayed on the corresponding KPFM image (Figure 4.1 b). In Figure 4.2, a analogue procedure was applied to the second sample on which the corrosion testing was done.

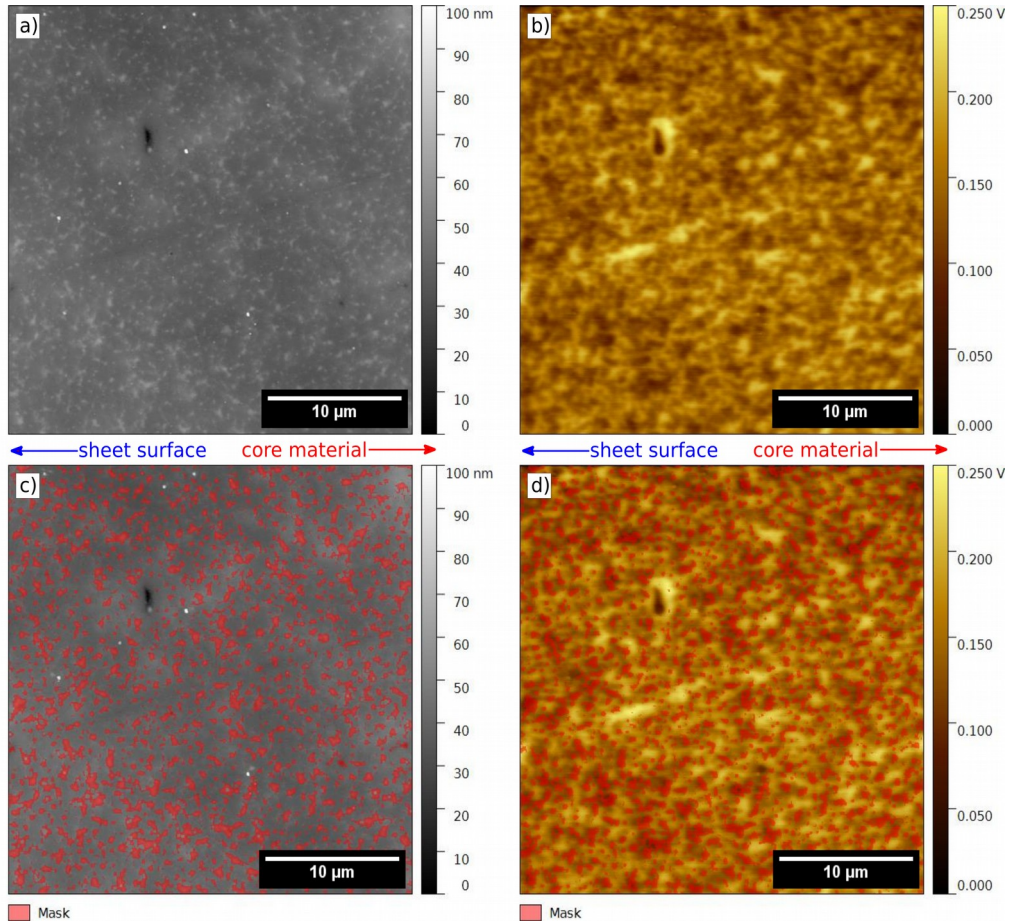


**Figure 4.1:** KPFM images for the intermediate layer of the 0 h sample. a) Topography and b) the corresponding CPD-map. c) The obtained mask of the topography map which was then applied to the CPD-map d).

As a reminder, the examination was done on two samples, because of the paste used for electrically grounding the sample during the KPFM measurement (see chapter 3.2). Values under the masked areas like the minimal and maximal bounding size, the minimal circumcircle radius, the maximum inscribed disc radius, and the minimal and maximal height of the structures were extracted via the “Grains > Distribution” tool. These values were then processed with the Libre Office Calculator to eliminate wrong markings. Those were recognized through a height (difference of the maximal z value and the minimal z value) of 0 nm. After this procedure, the statistical analysis could be performed with “Python(x,y)”. Values for the CPD-differences were obtained by overlaying the mask, obtained from the topography image, with the CPD-map and also extracting the minimal CPD of the grains.

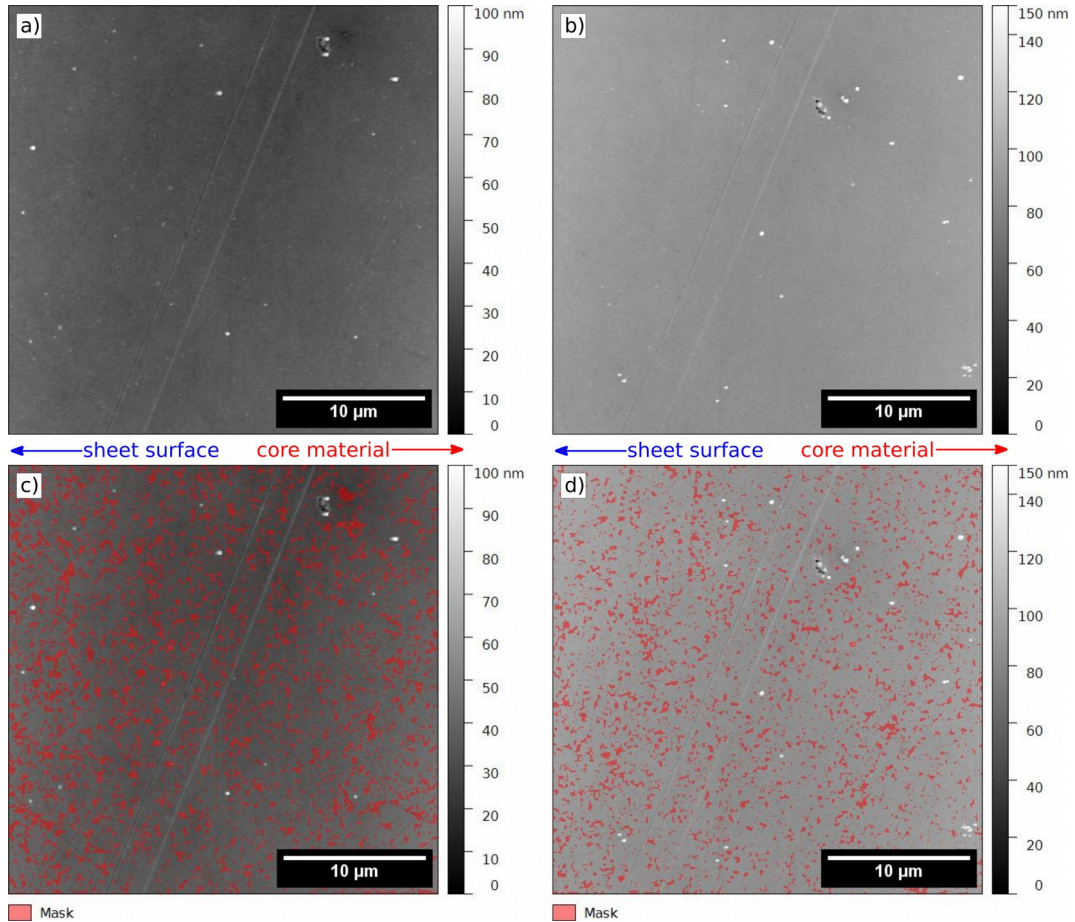


**Figure 4.2:** Topography images for the intermediate layer of the corrosion sample. a) Flattened topography for 1 h in the solution and b) flattened topography for 3 h. c) Mask for evaluation after 1 h immersion and d) after 3 h

For the value of the matrix, another mask was placed over the CPD-map, where the threshold was the height. This was necessary, since most of the surface areas were in some kind influenced by inclusions and only some small areas which had a higher difference to the CPD of the inclusions could be used as a matrix reference. An example for the mask placement can be seen in Figure 4.3. From these data, the mean value of the minimal CPD of the matrix areas was calculated and used to determine the CPD-difference of the inclusions with respect to the matrix.

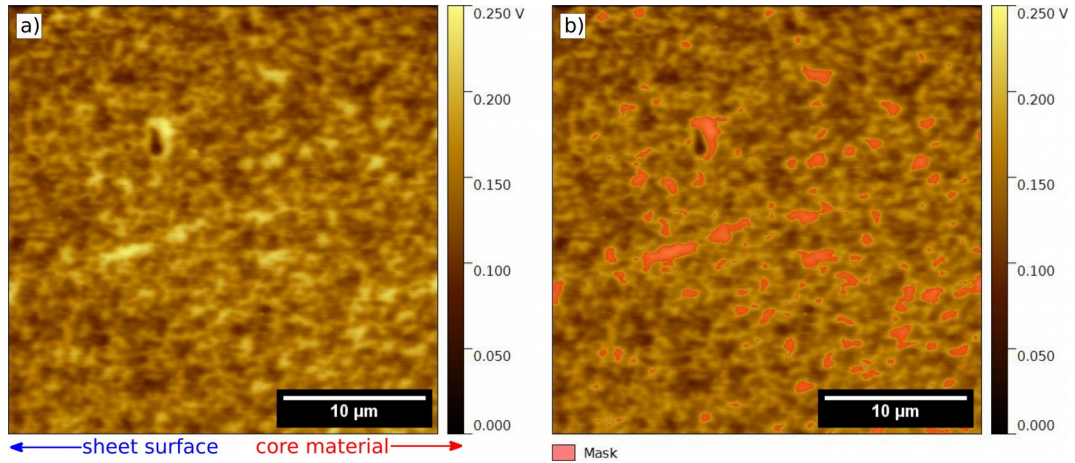


**Figure 4.3:** Example for the mask placement, through which the matrix CPD was obtained. a) CPD-map and b) the areas with the least influence from inclusions are marked for the matrix reference.

The projected area of this inclusion type and the CPD values were used to create histograms. They are summarizing inclusion size and CPD distribution and reveal how these distributions change during the corrosion process (Figure 4.4). It can be seen that the distribution of the projected area seems to follow nearly a log-normal distribution, whereas the CPD-difference between matrix and minimum CPD of the inclusion are normally distributed (Figure 4.4 b). The average size of the inclusion seems to diminish with ongoing corrosion. This is visible on the mean value for the mean area of the inclusions, on the first sample the mean area is  $15 \mu\text{m}^2$  and on the second sample after 3 h immersion testing it is only  $0.04 \mu\text{m}^2$  on the intermediate layer. It has to be mentioned that the obtained CPD of the inclusions are higher than the real CPD, because of the influence from the surrounding matrix area on the KPFM measurements. Because the development of the holes starts next to inclusions and the existence of a distinct CPD-difference between matrix and inclusions, it can be concluded that a small galvanic cell is formed which leads to a dissolving of the matrix in direct contact with the inclusions. At the beginning of the test, the biggest inclusion under the mask had an area of  $3 \mu\text{m}^2$ . After 1 h in the solution, the maximum area was  $1.86 \mu\text{m}^2$  for the second sample, even if the change is significant some doubt remains, because it is not the same sample. After 3 h in the solution the maximum area is reduced even more to a value of  $0.91 \mu\text{m}^2$ . For analytical reasons, it is also interesting to check if there is a direction dependent variation of the matrix-CPD. This was evaluated in Figure 4.5 using the “extract profile” tool, where three profiles with a width of 86 pixels (matching  $5 \mu\text{m}$ ) to reduce the influence from inclusions were extracted in the fast scan (Figure 4.5 a) and the slow scan direction (Figure 4.5 b). The fast scan direction is the direction in which

each line of the line by line scan from the AFM is made, the slow scan direction refers to the direction in which the measured lines are arranged next to one another to produce the image.

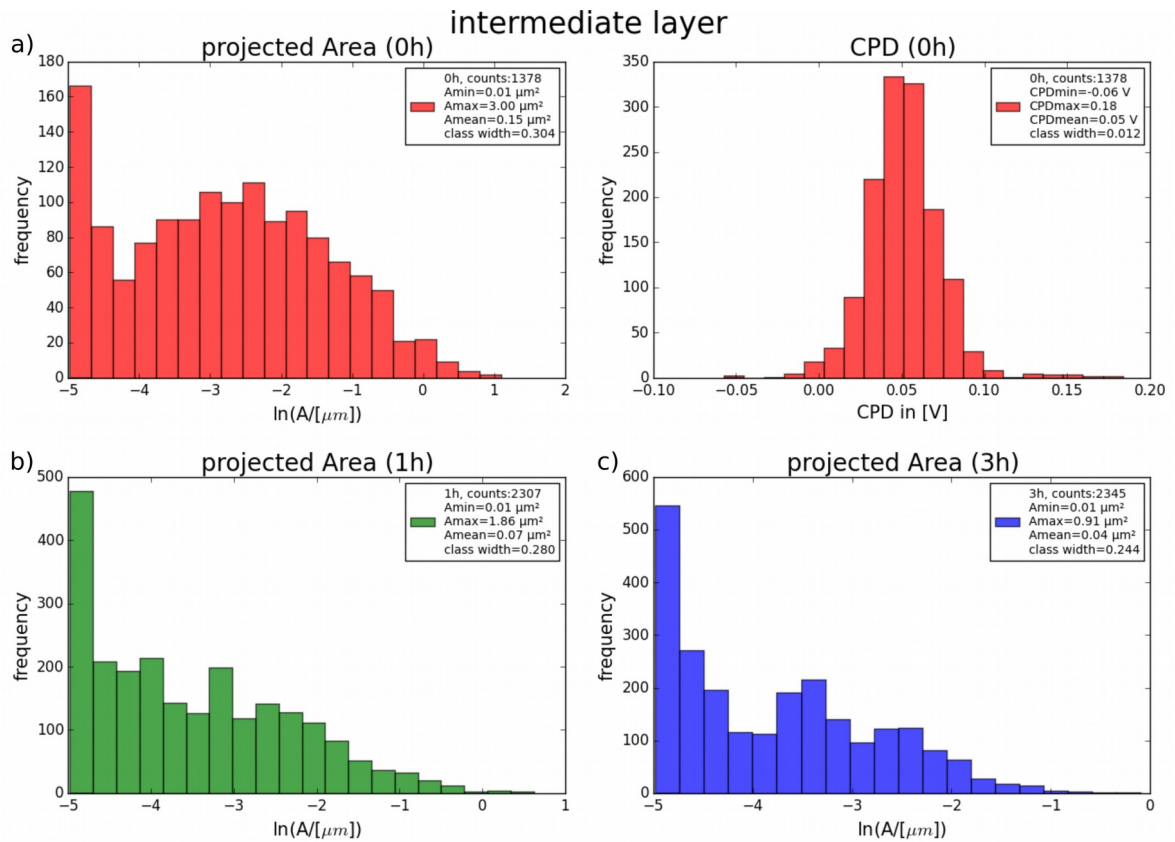


**Figure 4.4:** Results of the statistical evaluation of the projected area of the inclusions, as an indicator for their size, for the intermediate layer a) 0 h, b) 1 h and c) 3 h in solution. In a) additionally the CPD distribution is presented on the right. Counts in the legend is the total number of observed inclusions,  $A_{\min}$  is the smallest projected area of the analyzed inclusions ( $0.01 \mu\text{m}^2$  because of the resolution of the measurements), while  $A_{\max}$  is the largest.  $\text{CPD}_{\min}$  and  $\text{CPD}_{\max}$  refer to the highest difference between the measured inclusion CPD and the matrix-CPD value.

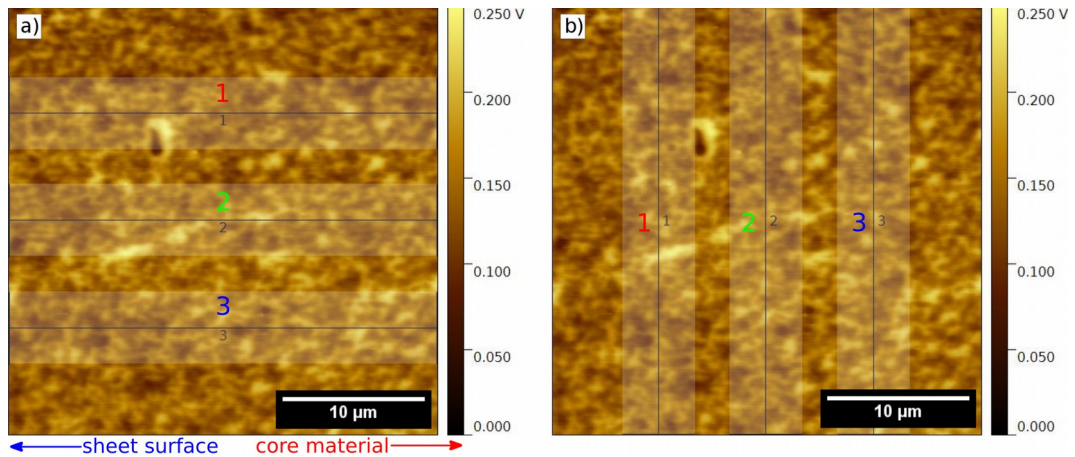


**Figure 4.5:** Direction dependent CPD-analysis of the KPFM image presented in Figure 4.3 a. a) Fast scan - b) slow scan direction. Semi-transparent white bars are used for width illustration, the numbers correspond to the lines presented in Figure 4.6.

From these three profiles, the average values were calculated and plotted. The results for the intermediate layer are presented in Figure 4.6.

There is a slight increase in the fast scan direction (Figure 4.5 a) from left (surface direction) to right (to the core material), and in the slow scan direction (Figure 4.5 b) from the top to bottom in the layer. This is indeed expected, because the material gets more reactive towards the center of the brazing sheet, and the fast scan direction doesn't align perfect with the shortest direction to the core material. Surprisingly, here the slow scan direction has the higher slope. The same analysis was made in the core material and on the border of the core material and intermediate layer and can be seen in the appendix. The highest slopes were on the border, with  $1.15 \text{ mV}/\mu\text{m}$  for the fast scan and  $1.06 \text{ mV}/\mu\text{m}$  in the slow scan direction. For the core material, the slopes were  $0.49 \text{ mV}/\mu\text{m}$  in the fast scan and  $0.78 \text{ mV}/\mu\text{m}$ . These results are in the same order as estimated, border > core material > intermediate layer.

Also the RMS roughness of the measured topographies were extracted via the statistical quantities tool of Gwyddion. The results can be seen in table 4.1.

**Table 4.1:** RMS roughness of the Al99.85 measurements.

results in nm	intermediate layer	border area	core material
0 h (sample 1)	4.0	16.1	33.1
1 h (sample 2)	4.4	28.9	67.7
3 h (sample 2)	4.4	21.4	65.6

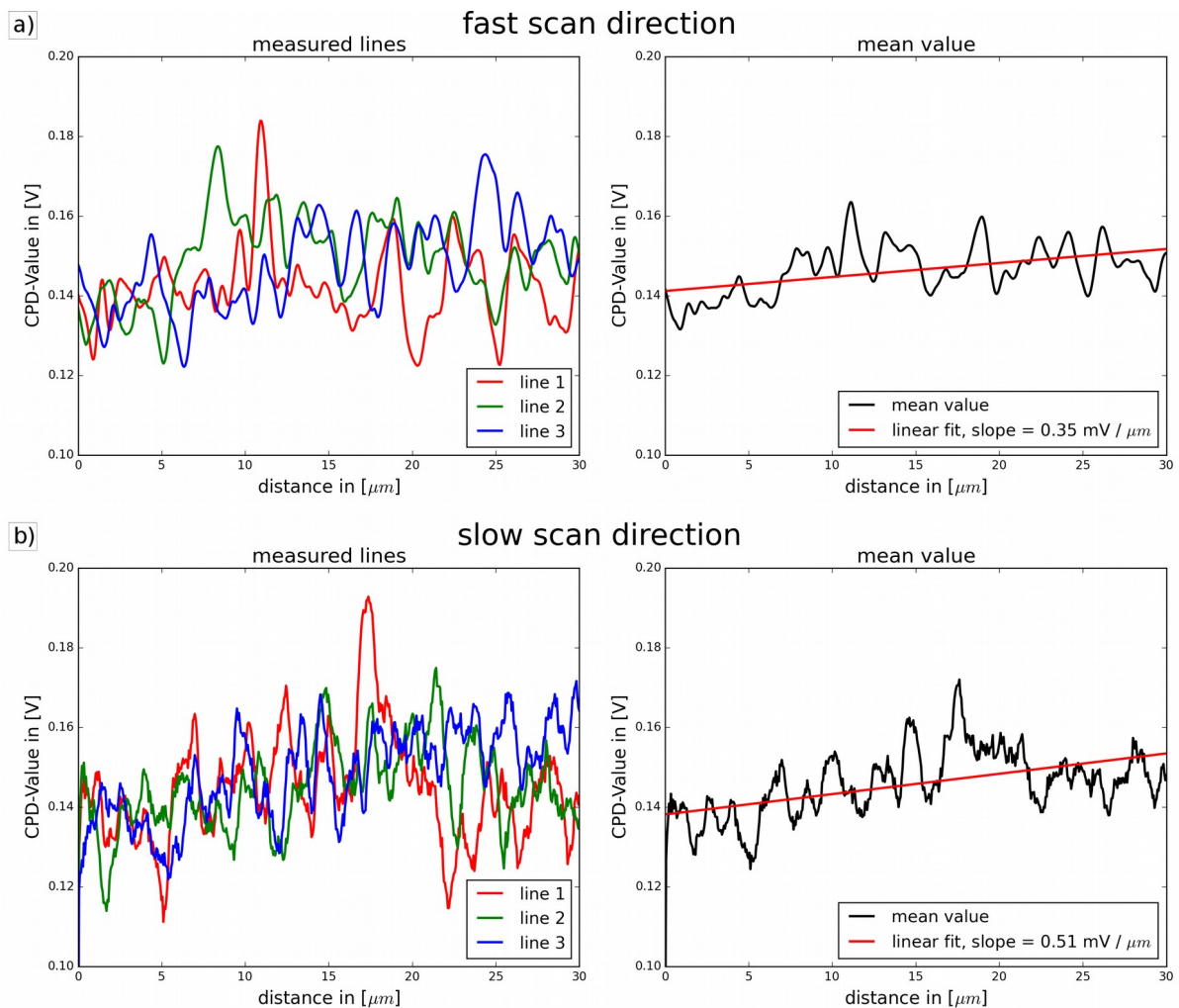


**Figure 4.6:** Line profiles extracted from the CPD-map of the intermediate layer. On the left side the originals are presented, a) in fast scan direction, b) in slow scan direction. On the right side, the mean values of the three extracted profiles are shown together with a linear fit and the resulting slope.

For the KPFM sample (0 h) the roughness is explainable through the polishing steps and the different heights of the inclusions. Only very small inclusions are in the intermediate layer until the border, where some bigger inclusions can be found. Whereas in the core material are mainly bigger ones contributing to the RMS roughness. This means the RMS roughness is directly connected to the size of inclusions on polished surfaces. Higher values after immersion testing at the border area and core material are consequences of the corrosion process and the insufficient cleaning (holes and corrosion residues).

## 4.2 Examination of AlSi10/AlMn1/AlZn4.5Mg1

The main focus for this sample was on the Al(Fe,Mn)Si inclusions. Their dimensions were evaluated with regard to height, the minimal circumcircle radius, and the maximum inscribed disc radius. Further, the CPD-difference between matrix and inclusions was recorded. However, this was not always possible because of the disturbing influence of the corrosion products. A similar analyzing procedure as for the Al99.85 sample was employed. A mask was placed on the topography image via the “Mark by Threshold” tool, where the slope and the height were used together as parameters. The resulting mask was modified by erasing smaller parts with the “freehand erasing” command and filling the gap between the lower and higher parts of the marked inclusions by the “fill continuous empty areas” command of the “Mask Editor” tool. The desired properties were extracted via “Grains > Distribution”.

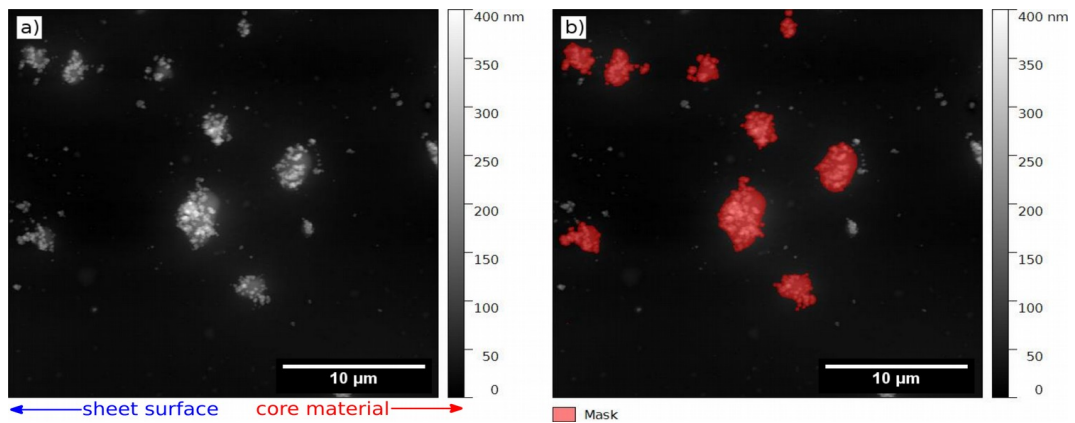


**Figure 4.7:** AFM images for the value gathering of the intermediate layer (AlMn1). a) the flattened topography before immersion testing, b) mask obtained through the procedure described in the text.

In Figure 4.7 an example of a mask obtained from the topography image can be seen. This mask was also placed on the CPD-map to evaluate the minimal CPD value of the inclusions, also with the “Grains > Distribution” function. Because of the long interaction range of electrostatic forces, it can be estimated that there will be an influence from the surrounding matrix material. Thus, the lowest measured CPD value on the inclusion is the one nearest to the real value. To obtain a matrix-CPD value a different mask was placed over the CPD-map with the height (75%) as threshold, and the minimal value under this mask was used as the matrix value. Figure 4.8 shows a CPD-map together with the two masks used for evaluation. The data obtained was then processed using a python program. First, the height range of the inclusions are calculated, by subtracting the minimal z - value from the maximal z - value. Then the CPD-difference range was calculated in a similar way



using the highest value of the matrix and the lowest value of the inclusions. For further investigation, the obtained data was filtered by size of the projected area ( $> 1 \mu\text{m}^2$ ) to reduce the influence of polishing residues and to focus on the bigger inclusions, and the type of masked characteristic (trough or inclusion). To characterize the accuracy of this method, it was assumed that all the inclusions should in principle exhibit the same CPD and only a difference in the lateral diameters leads to different CPD measurements (see Figure 2.7). In order to visualize possible correlations between CPD and inclusion size, the CPD-difference was plotted as a function of the maximal inscribed disc radius. An example for those plots is presented in Figure 4.9.

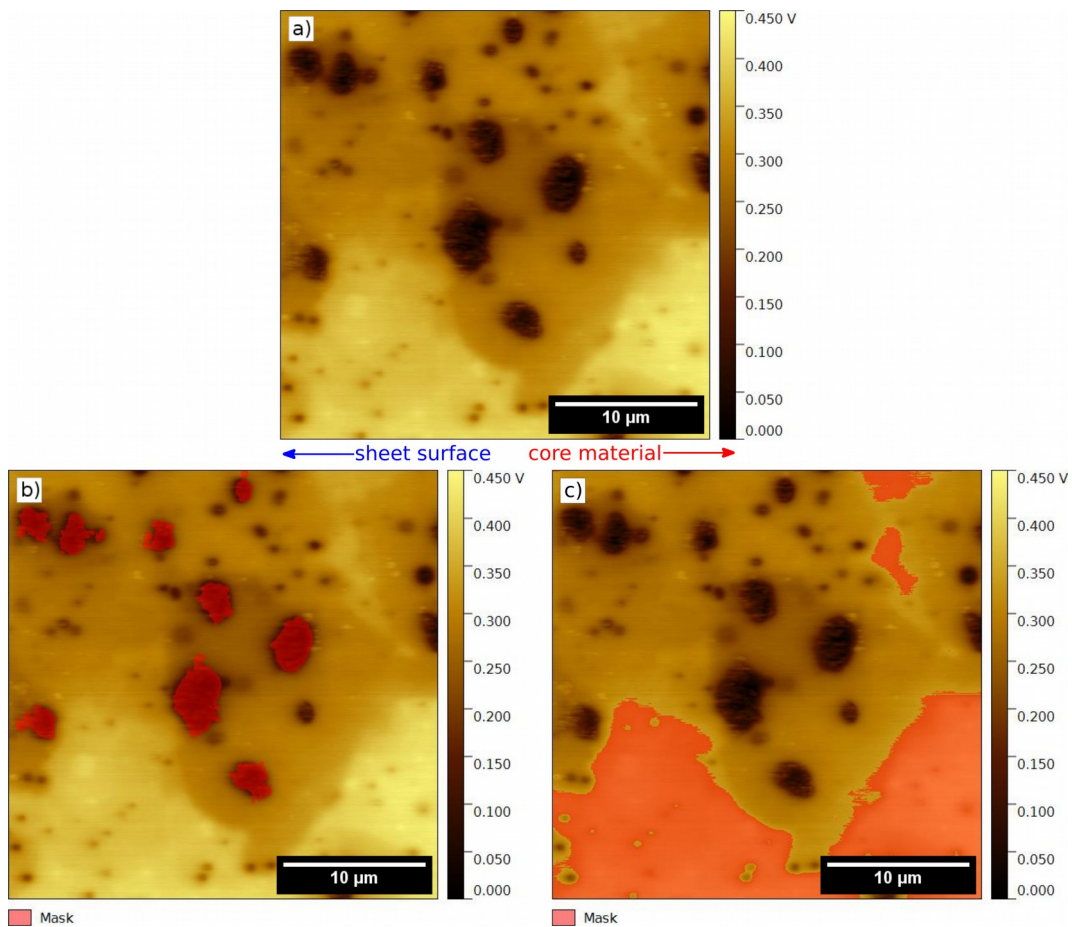
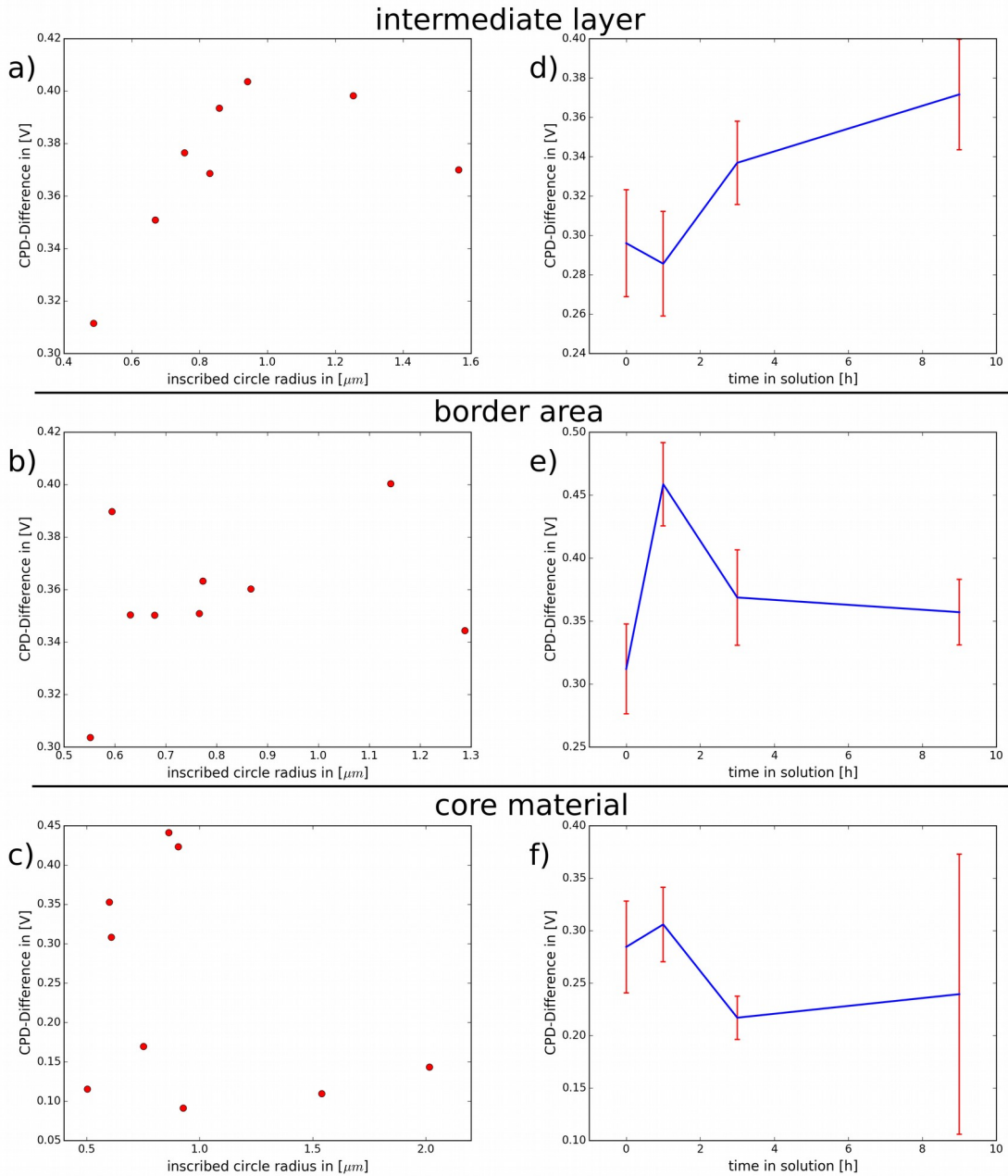


**Figure 4.8:** KPFM images for extracting CPD values of the intermediate layer (AlMn1). a) CPD-map of the intermediate layer as measured. b) KPFM image overlaid with mask from the topography (see Figure 4.7 b) to evaluate the inclusions. c) mask used for the matrix value.

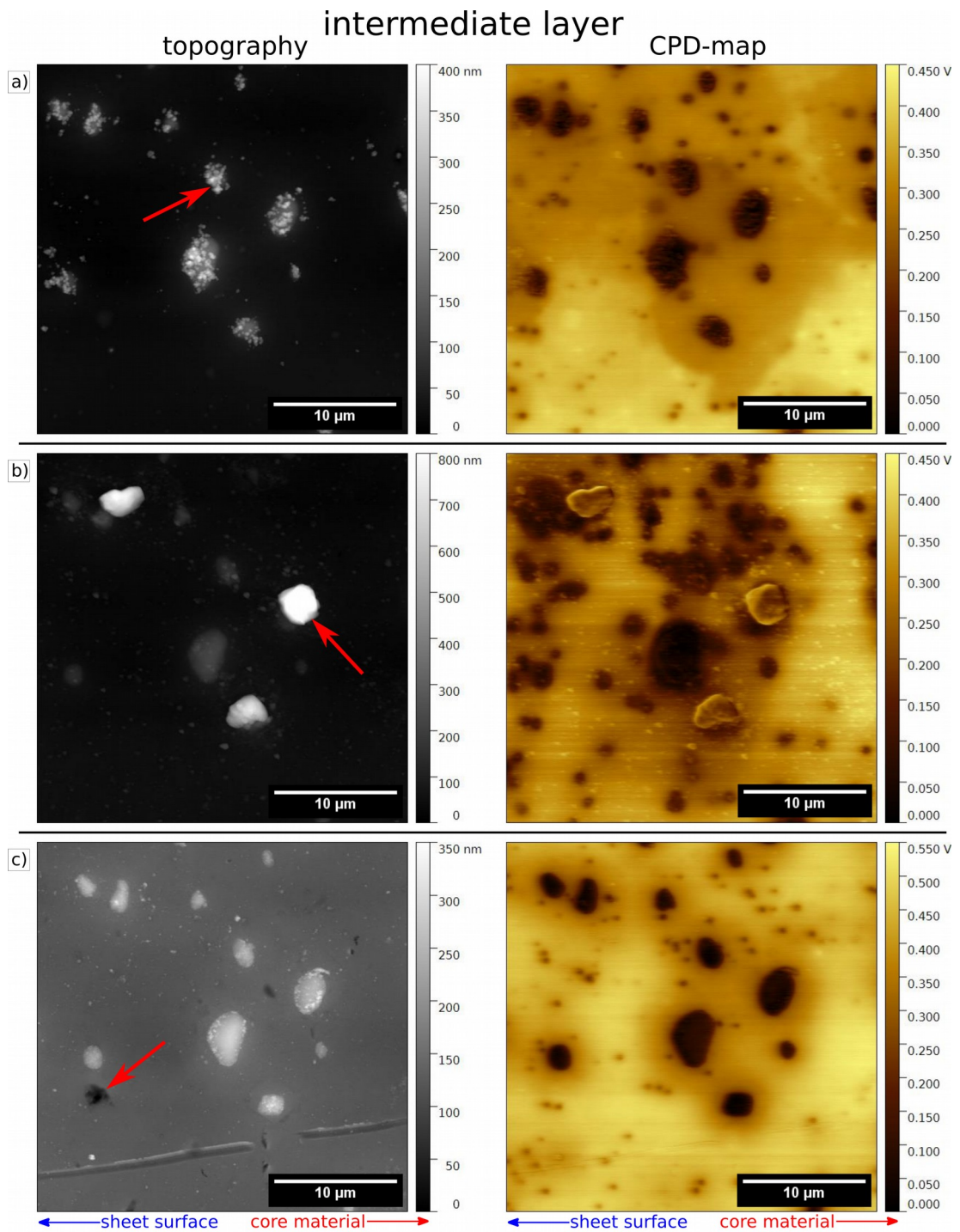
For small feature sizes, the real CPD of the inclusions was not measurable. However at least a trend is clearly visible. It seems that above an inscribed circle radius of  $1 \mu\text{m}$  the CPD is measured correctly, since the values don't change anymore (see

Figure 4.9 a). For the core and border materials, no clear trends with time are noticeable. In the intermediate layer, the CPD-difference increased after the 3 h mark. This rise seems to be correlated to the start of the pitting corrosion in this area, because the first heavy attack has been observed after 9 h immersion. The corresponding images are presented in Figure 4.10.

Figure 4.11 presents the effects of corrosion on the border area. Where in Figure 4.9 b), a small reduction of the CPD-difference between inclusions and matrix after an initial raise at the 1 h mark could be detected. This CPD-difference increase after 1 h exposure can be attributed to the removal of polishing residuals. After 3 hours in the solution, a conglomeration of corrosion products could be observed on the bottom right of the picture where the measured CPD was high (indicated by a red arrow in Figure 4.11 b). A hole could be found at the same place after combined 9 hours of immersion testing. In the CPD-map of Figure 4.11 a) a border is visible through different matrix-CPD values. Next to this border a through is forming during the immersion testing. The behavior of the CPD-differences of the core material was similar to the one of the border layer, the values for the 3 hours mark are speculative, because of the heavy contamination through corrosion products and probable residuals from cleaning with isopropanol. As for the intermediate layer by the 9 hour mark, an increase in the difference was observed, but this time without signs of increased corrosion.



**Figure 4.9:** CPD-difference between Al(Mn,Fe)Si inclusions and matrix are shown. a) to c): CPD-difference versus inscribed circle radius after 9 h in solution, d) to f): mean CPD-difference changes versus time in solution. a) and d) for the intermediate layer. b) and e) for the border area. c) and f) for the core material. Error bars indicate the standard deviation of the inclusions CPD-differences.



**Figure 4.10:** Topography image (left) and CPD-map (right) of the intermediate layer a) after polishing, b) after 1 h, and c) after 9 h immersion testing. The red arrows indicate a polishing residue in a), an undefined surface pollution in b), and a trough generated by corrosion in c).

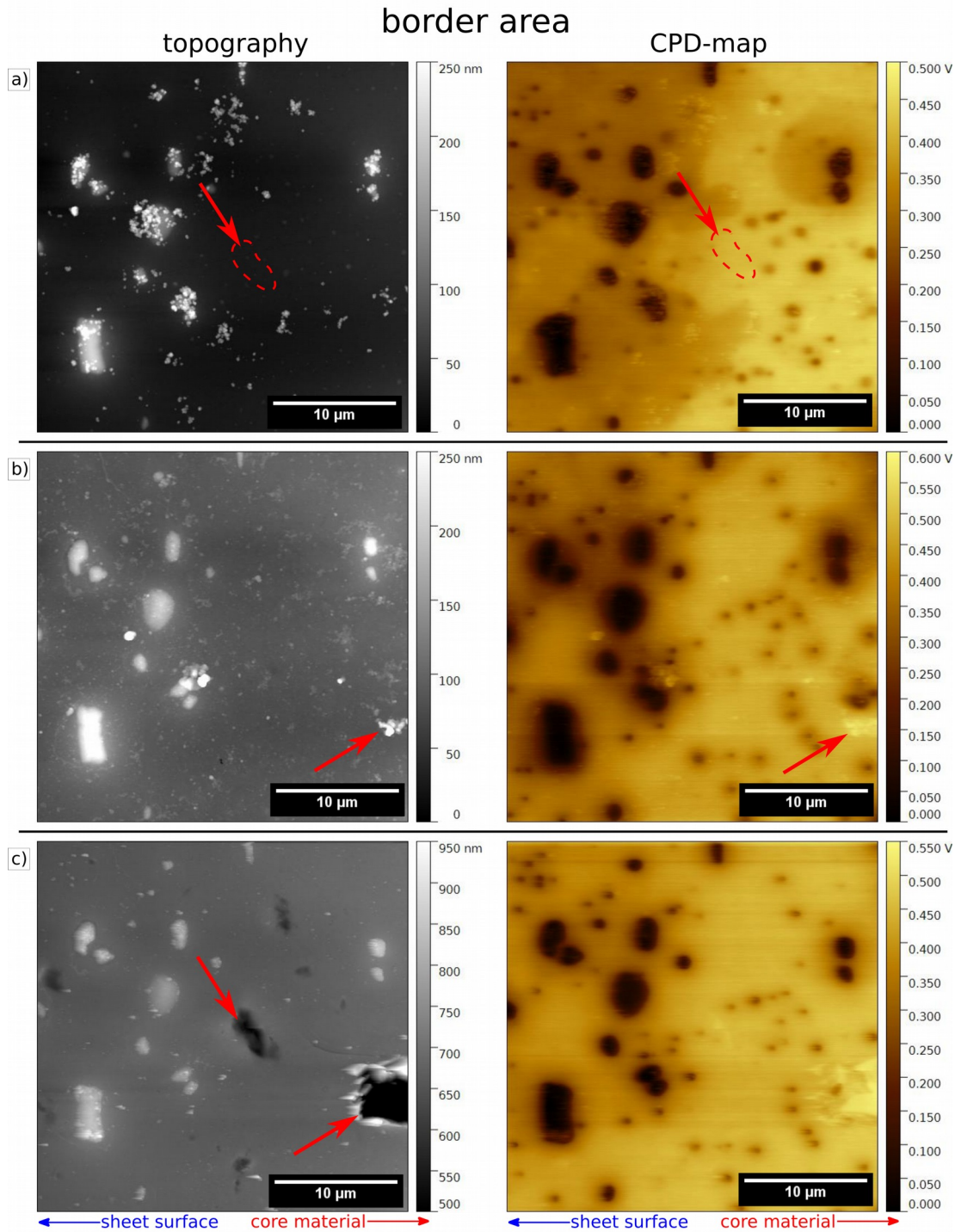


**Figure 4.11:** Topography image (left) and CPD-map (right) of the border area a) after polishing, b) after 3 h and c) after 9 h immersion testing. In a), the same polishing residuals as in Figure 4.10 can be seen. The trough next to the border (seen in c)) is marked by a dashed line. In b), a film of corrosion products is apparent, and the conglomeration which started the development of a hole in c) is marked. c) shows troughs along the border and the hole caused by the conglomeration seen in b).

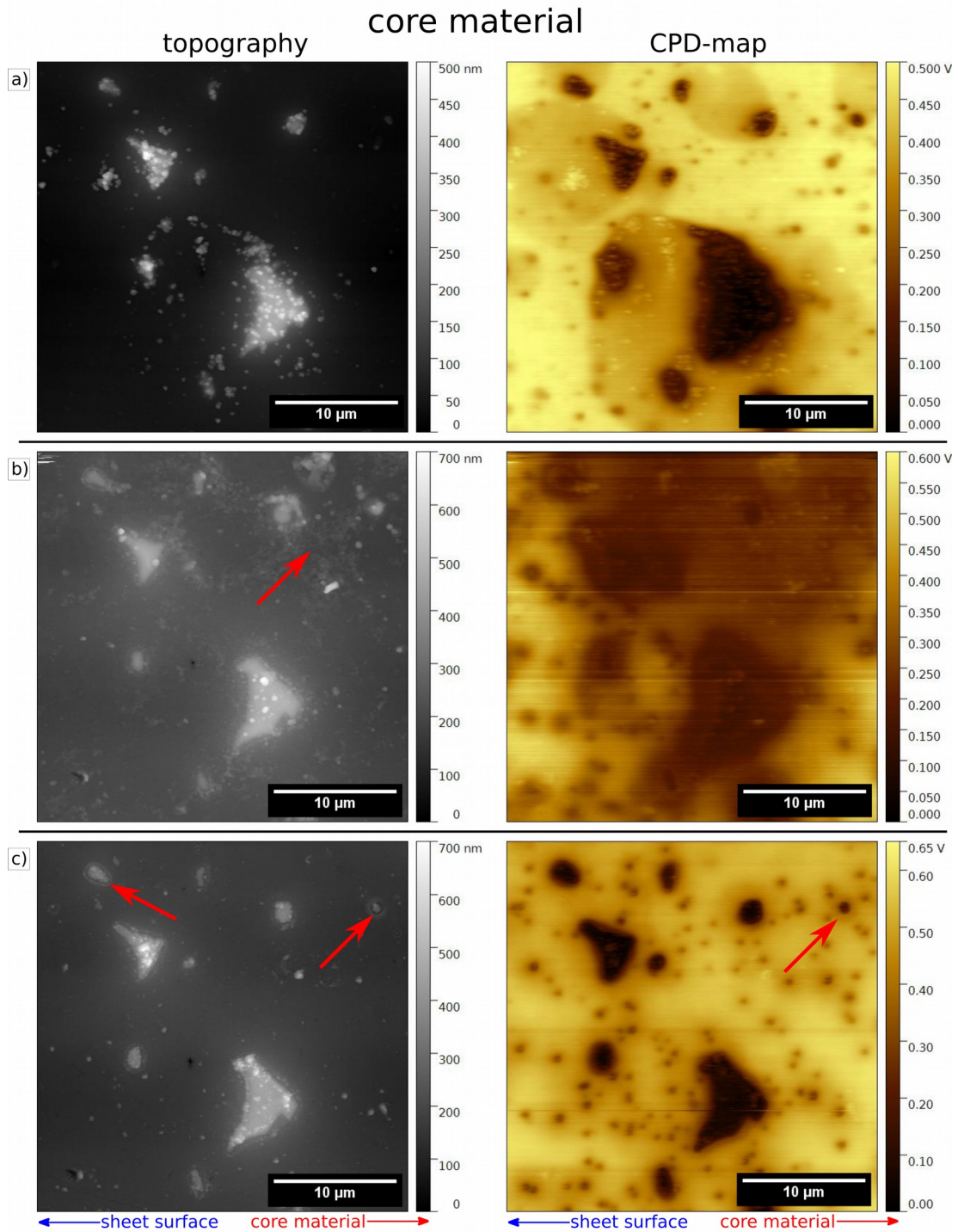


**Figure 4.12:** Topography image (left) and CPD-map (right) of the core material a) after polishing, b) after 3 h, and c) after 9 h immersion testing. In a), the same polishing residuals as in Figure 4.10 can be identified. In b), a film of corrosion products and cleaning residues is apparent, and the effects caused by it can be recognized in the CPD-map. In c), the corrosion of the material around the inclusions is well visible.

In the core material, the dissolution of the material around the inclusions can clearly be seen. This will cause the inclusions to detach after prolonged corrosion. In Figure 4.12 the results for the core material are presented. In all three areas, it was possible to observe that after the first hour of immersion testing the corrosion products were mostly placed around inclusions and that the formation of corrosion troughs was always found in areas adjacent to inclusions.

As with the Al99.85 sample the RMS roughness of the surveyed surface was extracted and the results can be seen in table 4.2

**Table 4.2:** RMS roughness of the AlMn1 measurements.

results in nm	intermediate layer	border area	core material
0 h	32.5	29.9	57.2
1 h	97.0	25.3	51.1
3 h	36.7	26.2	57.5
9 h	23.1	56.7	58.4

The bigger RMS roughness changes can be traced back to the change of pollution through residuals. At the initial measurement (0 h) polishing residues were on the surface which influence the CPD-difference and the RMS roughness measurements. These residuals were washed of during the immersion testing, which led to a higher CPD-difference and lower RMS roughness for the border area and core material. The significant jump from 26.2 nm to 56.7 nm on the last two measurements of the border area are due to the formation of holes. On the intermediate layer a undefined pollution could be detected, which can be deduced as the reason for the higher RMS roughness and lower CPD-difference after 1 h immersion, and the drop between the 3 h measurement and 9 h mark is because the surface was cleaner on the last measurement, which resulted in a lower RMS roughness, even with the forming holes.

In order to speculate on a possible reason for the changes of the CPD values of the AlMn1 sample, an chemical analysis by scanning electron microscope (SEM) through energy dispersive X-ray analysis (EDX) was done, on a newly prepared sample. First, a suitable area was selected, where the possibility for observable corrosion was high. Then an EDX measurement was carried out on the inclusions and in the areas around them. After an immersion test of 3 hours, the same area was measured a second time, in order to find distinct differences of the results from the first EDX measurements. Results for the intermediate layer can be found in table 4.3 and the corresponding SEM images are shown in Figure 4.13. In addition to the elements

presented in table 4.3, after 3 h of immersion 0.7 – 1.0 wt% Cl was found on the sample.

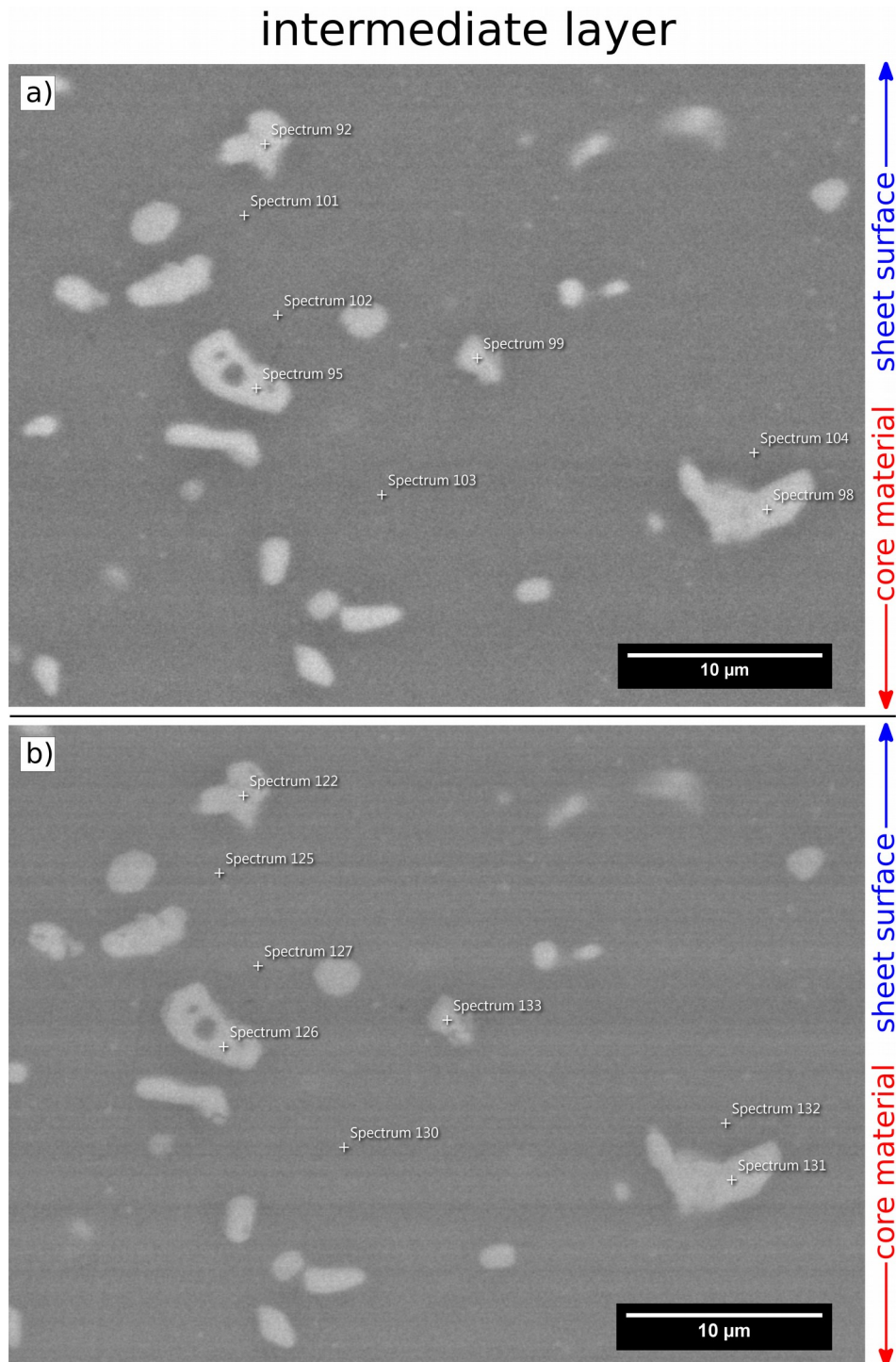


**Figure 4.13:** SEM image of the intermediate layer, with the marked positions for a spot EDX measurement. a) before the immersion test and b) after 3h. No clear sign for corrosion could be detected.



**Table 4.3:** EDX-results of the intermediate layer in weight percentage [wt%] for the spots marked in Figure 4.13. In all 3 h measurements, 0.7 to 1.0 wt% Cl was detected.

Spot Nr. 0h	Al [w%]	Mn [w%]	Fe [w%]	Si [w%]	Zn [w%]	Spot Nr. 3h	Al [w%]	Mn [w%]	Fe [w%]	Si [w%]	Zn [w%]
92	79.9	8.3	6.5	4.2	1.1	122	78.6	8.3	7.0	4.1	1.1
101	96.9	0.9	0.6		1.6	125	96.1	0.7	0.4		2.0
102	97.2	0.7	0.3		1.7	127	96.0	1.0	0.5		1.7
95	81.9	7.1	6.0	3.7	1.4	126	81.3	7.0	6.3	3.2	1.4
103	97.2	0.6			2.2	130	96.2	0.7			2.3
99	92.7	2.3	1.3	1.9	1.8	133	96.2	0.6	0.3		2.0
104	97.3	0.4			2.2	132	94.6	1.6	1.0		1.9
98	80.9	6.6	7.8	3.3	1.3	131	78.2	8.8	7.4	3.5	1.3

It was uniformly distributed for all spots of the measurements. Thus, an effect on the observed CPD changes is not very likely. The obtained results didn't reveal a big difference of the chemical compounds between the first and the second EDX measurement, but the same corrosion behaviour as for the AFM-tests could be observed. However in the intermediate layer nothing is seen after 3 h immersion, as was shown in Figure 4.13. The core material has pits, and the corrosion takes place next to the inclusions, as found in Figure 4.14.

**Table 4.4:** EDX-results of the core material in weight percentage [wt%]. In the 3 h measurements, Cl was detected in a range of 0.8 to 2.0 wt%.

Spot Nr. 0h	Al [w%]	Mn [w%]	Fe [w%]	Si [w%]	Zn [w%]	Mg [w%]	Spot Nr. 3h	Al [w%]	Mn [w%]	Fe [w%]	Si [w%]	Zn [w%]	Mg [w%]
106	87.0	1.1	5.7	2.2	3.3	0.7	141	85.0	1.0	6.8	2.0	3.1	
111	94.3		0.6		4.2	0.9	145	93.8				4.5	0.9
107	79.5	1.2	13.5	2.8	2.9		142	78.7	1.1	13.9	2.8	2.7	
109	94.4	0.3	0.5		4.0	0.8	144	91.2	0.6	2.1		4.3	0.9
108	81.9	1.0	11.4	1.6	2.8	0.6	143	80.5	1.1	12.8	1.3	2.9	
110	94.6				4.4	1.0	146	92.9		0.6		4.7	0.9

The measurement suggests that no preferential removal of certain elements of the alloy in the core material occurs due to corrosion. This would be visible by a relative decrease of this element. Therefore the observed strong corrosion along the inclusions is likely to be a galvanic coupling effect. The stronger dissolution in comparison to the AFM/KPFM testing, visible in Figure 4.12, can be explained through the testing procedure. In this experiment, the sample was only removed once from the corrosive solution after 3 h, whereas in the AFM/KPFM experiment the

sample was removed after 1 h and after 3 h. Most likely, the protective oxide layer of the Al-alloys has been renewed, which results in a lower corrosion rate for the previous measurement (by AFM).

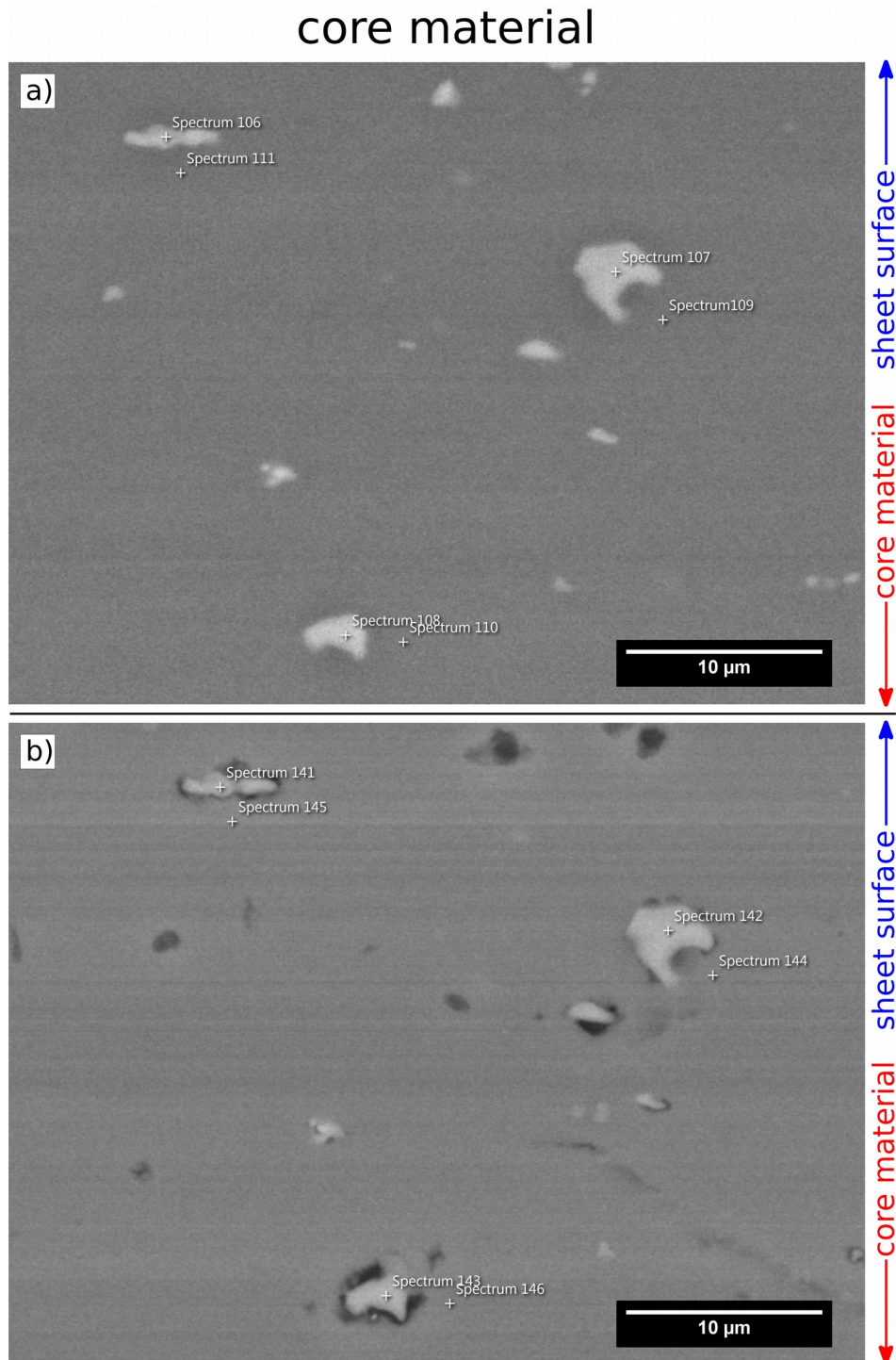


**Figure 4.14:** SEM image of the core material, with the marked positions for a spot EDX measurement. Left before the immersion test and right after 3 h, clear sign for corrosion can be seen around the inclusions, and some pits are visible, where inclusions were dislodged.

## 5 Discussion

At first, the differences of the results for the two used brazing sheets after the 3 h immersion testing will be discussed. Because of the different intermediate layer, a big difference in the corrosion behavior in this layer was expected. However Figure 5.1 demonstrates that the visible attack was in in the same range of damage, and no significant difference in the dissolution of the matrix is noticeable. The matrix preferentially dissolves next to smaller inclusions. For bigger inclusions, the effect is less pronounced. However, for the AlMn1 layer trenches of around 3 to 15 nm are forming around the bigger Al(Mn,Fe)Si inclusions. In Figure 5.2, the resulting topography for the border areas between intermediate layer and core material are shown. Here, a clear difference between the samples can be seen. In the sample with the AlMn1 layer, only a small degree of corrosion is visible (next to little inclusions and around bigger Al(Mn,Fe)Si ones). In contrast, for the Al99.85 layer, a clear line of holes in the border area along the interface of the intermediate layer and core material is visible. This line of holes can be explained through the different distribution of the inclusions as well as the change of the CPD from the intermediate layer to the core material. Even though there is no sharp transition of the CPD in this area (because of a homogeneous diffusion and the resulting distribution of the alloying elements in the matrix [1],[9],[10]) the change in the CPD together with the frequent occurrence of inclusions along the border seem to have a detrimental influence on the corrosion behavior and can lead to delamination on the macroscopic scale. It has to be mentioned, that the line of holes was already established after 1 h of immersion. In the core material, which is the same in both samples, the same traces of attack can be observed on both samples. A dissolution of the matrix paired with a deposition of corrosion residues around the inclusions. A comparison of the two samples is shown in Figure 5.3.

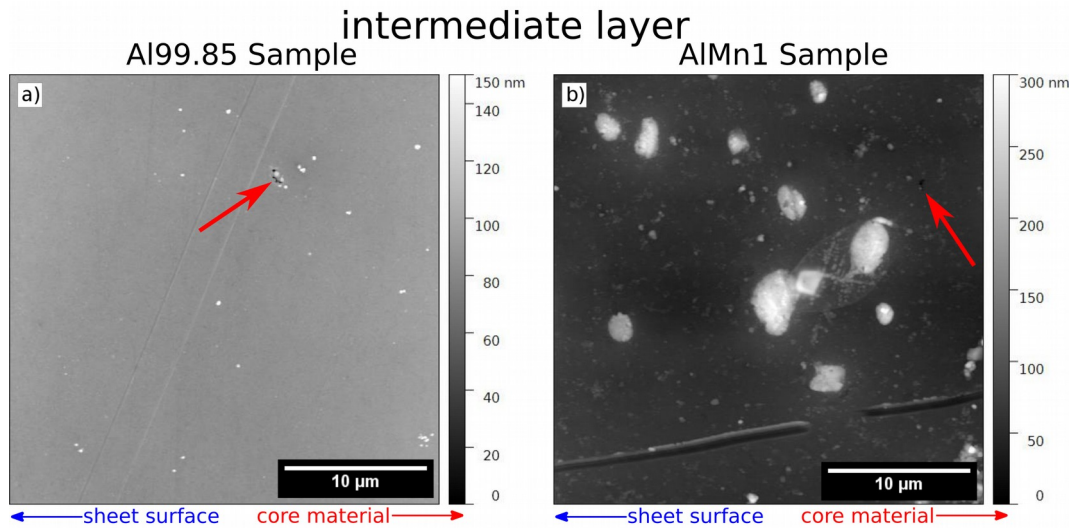


**Figure 5.1:** Topography images of the intermediate layer for the two immersion testing samples after 3 h immersion. a) Sample with the Al99.85 intermediate layer, b) sample with the AlMn1 layer. In both images, the start of a mould next to an inclusion is marked.

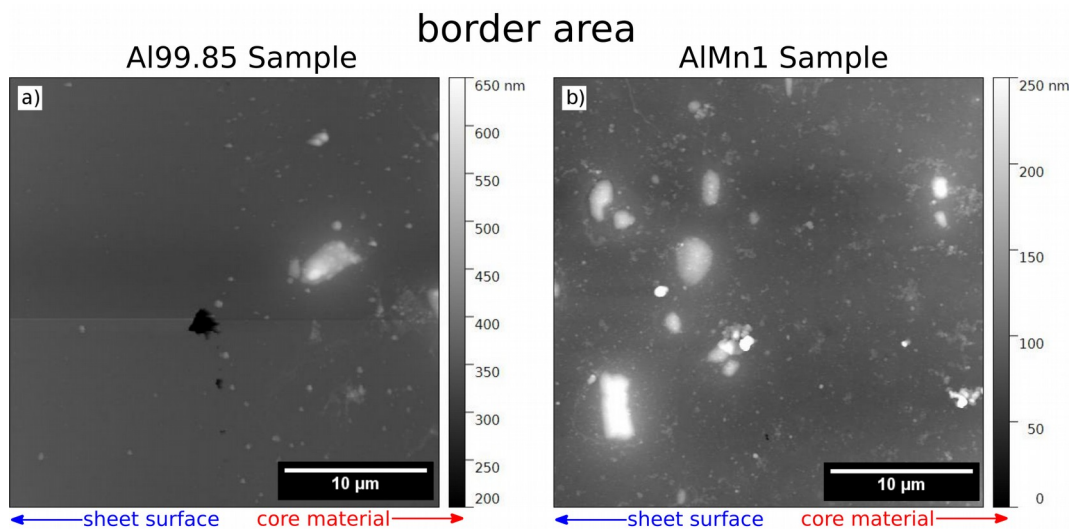


**Figure 5.2:** Topography images of the border area of the two immersion testing samples after 3 h immersion. a) sample with the Al99.85 intermediate layer, b) sample with the AlMn1 layer. The intermediate layer is in both pictures to the left, which is easily seen in a). A line of holes along the interface of the core and intermediate layer is visible in a), whereas only a small hole is formed in b).

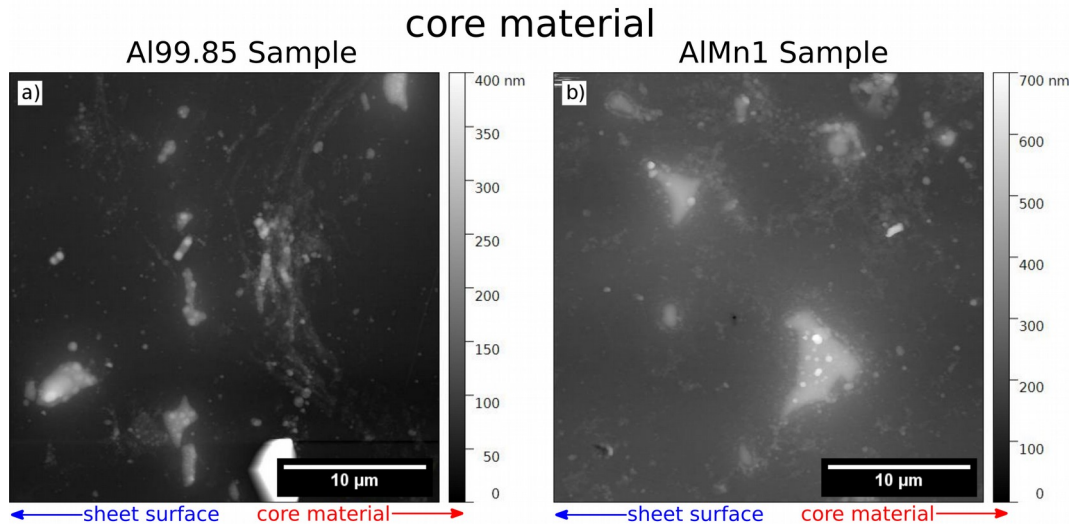


**Figure 5.3:** AFM Topography images of the core material of the two immersion testing samples after 3 h immersion. a) Al99.85 intermediate layer and b) the AlMn1 intermediate layer. Corrosion residues around the inclusions are visible, as well as small moulds in b).

In Figure 3.2, it is visible that in case of the Al99.85 sample the area for the core material measurement was close to the border region, whereas for the AlMn1 sample the inspected core area is at a further distance to the border. This means that for Al99.85 an impact of the intermediate layer can not be completely excluded. From the measurement on the KPFM Al99.85 sample, a change of the matrix-CPD was observed in all three areas in the slow scan as well as the fast scan direction. The strongest variation was found at the border area (the corresponding CPD-profiles can be found in Figure 4.6 for the intermediate layer and in the appendix for border and core area). The CPD slope of the matrix in the intermediate layer and the core material are quite comparable. This CPD slope of the matrix can be considered as an indicator that the matrix is getting more reactive in the direction to the core material, and that a stronger corrosion attack can be anticipated in the core material. The CPD slope on the border area was higher than the other two, which indicates that the stronger diffusion occurs at the border, and the matrix is less homogenous. Thus, a higher susceptibility to corrosion is likely, because parts of the matrix could have a sufficient difference in the potential that a galvanic element can be formed, where the effect of the inclusions is minor. Thus, not only the matrix-inclusion interface can lead to corrosion but also "intrinsic" potential gradients in the matrix itself. These CPD measurements correlate quite well with the observed corrosion. At the border (see Figure 5.2 a), where the CPD slope is highest, a line of holes can be seen, whereas in Figure 5.1 and 5.3 only a small corrosion attack can be found next to inclusions. All

KPFM measurements yield a clear difference between the matrix and the inclusions, whereas a reliable value for the CPD-difference could only be obtained for inclusions bigger than an inscribed circle radius of 1 $\mu$ m. The measured CPD-difference of 300mV of the 0 h samples is in good agreement with the results from [32] which shows results for  $\alpha$ -Al(Mn,Fe)Si inclusions also in the region of 300 mV. The CPD-difference together with the corrosion behaviour are a clear indicator for a galvanic process, where the matrix is the anodic part and the inclusions support the cathodic reaction.

The matrix - inclusion galvanic coupling would suggest to use the Al 99.85 for the intermediate layer. However, because of the strong change in the CPD of the matrix in the border area the advantage of reduced corrosion in the intermediate layer is compensated by the risk of delaminating the intermediate layer from the core material. In contrast, the more homogenous corrosion behavior of the AlMn1 makes AlMn1 more suitable for this kind of sheet.

The change of the CPD-difference between matrix and inclusions during the corrosion testing, which was observed on the AlMn1 sample, could have different reasons. One would be the diminishing of the protective oxide layer, which might change its thickness, and/or its structure. This can result in a higher CPD-difference. Another possible explanation would be the selective dissolution of elements in the inclusions or the matrix. Anyway, the results of SEM/EDX measurements do not support this possibility, which can therefore be ruled out. A last possible explanation could be a thin film of corrosion residues together with residues from the immersion liquid that cover the surface. This could cause a highly active film. Something like this can be seen in Figure 4.12 where a conglomeration of residues causes a higher CPD value and a formation of a hole during ongoing immersion testing. Further, the SEM/EDX measurements reveal that Cl is evenly distributed on the surface, which can be caused through the infiltration of pores of the oxide layer and/or residues from the immersion testing. But it is not possible to state, if the effect on the CPD is the same for the matrix as for the inclusions.

## 6 Summary and outlook

For this work an AFM and KPFM investigation was done on two high-strength aluminium brazing sheets. Both sheets had the same AlZn4.5Mg1 core material and AlSi10 brazing layer, but did differ in the intermediate layer. The first sample had an Al99.85 intermediate layer, whereas the second sample had an AlMn1 intermediate layer. The aim was to examine the corrosion process occurring in a modified SWAAT solution in fixed time intervals by AFM and compare the results with an initial KPFM measurement. It can be summarized that from the two used intermediate layers the Al99.85 was more or less evenly corroded, whereas for the AlMn1 layer a pit formation happened. Further, it was observed, that the Al99.85 border more strongly trends to delamination, than the AlMn1. As well, it could be demonstrated that the inclusions in both brazing sheets are cathodic in nature to the aluminium matrix. The observed Al(Mn,Fe)Si inclusions found in the core material and in the intermediate layer on the AlMn1 sample showed a CPD-difference of around 300 mV to the Al-matrix. Also it could be seen that the measured CPD-difference of the inclusions is dependent on the inclusion size. The size dependence can be explained through the long-range interaction of electrostatic forces. On the samples for the Al99.85 intermediate layer, a slope of the matrix CPD was observed. The slope didn't align exactly along the predicted direction, from the surface to the core material. This can be because of an uneven distribution of the dispersoids, an inhomogeneous diffusion or an aligning failure for the fastscan axis of the AFM.

The fact that the inclusions act via cathodic way and the matrix metal anodic is already known [14]. However, important is that KPFM can be applied for an estimation of the local corrosion susceptibility and can therefore reduce the testing time and necessary equipment. The biggest problem encountered in this thesis, the corrosion residuals which can locally interfere with the measurements, are of no concern to the estimation of the corrosion susceptibility, because the measured surface doesn't need to be corroded. Basically, only the initial KPFM measurement is necessary.

This thesis was intended to be a feasibility study and did not focus on optimization of the measuring time. The time used for this measurement can be reduced, by employing FM-KPFM and a faster scanning speed. A less comprehensive study, only for performance enhancement could be performed, in which the measuring time, the used lift height, and the necessary measurement area could be optimized as well as the type of used probes.

In the framework of this thesis, one improvement of the testing procedure was

already implemented. The electrical contact of the sample at the backside, which lets the observed surface uninfluenced and usable for further testing. Other improvements could be obtained through a better cleaning step. So far, the sample was cleaned in a ultrasonic bath with isopropanol and rinsing afterwards also with isopropanol. This still left some residuals on the surface, which made the measurements more difficult. A minimal value for the CPD-difference which is necessary for corrosion to start could not be found, and is most likely not possible to be obtained precisely.



## List of references

1. S. Tierce, N. Pébère, C. Blnc, G. Mankowski, H. Robidou, D. Vaumousse, J. Lacaze. Solidification and phase transformations in brazed aluminium alloys used in automotive heat exchangers, *Int. J. Cast Met. Res.* **18** (2005) 370-376.
2. F. Ostermann. "Anwendungstechnologie Aluminium", Springer-Verlag Berlin Heidelberg, 2007.
3. H. Oettel, H Schumann. "Metallografie", WILEY-VCH Verlag GmbH & Co. KGaA, 2011.
4. Dr. C. Kammer. "Aluminium Taschenbuch 1", Aluminium-Verlag Düsseldorf, 2002.
5. J. Gilbert Kaufman. "Properties of Aluminum Alloys", ASM International, 1999.
6. J.R. Davis. "Corrosion of Aluminium and Aluminium Alloys", ASM International, 1999.
7. I. Polmear. "Light alloys: from traditional alloys to nanocrystals", Butterworth-Heinemann, 2006.
8. J.-S. Ryu, M.-S. Kim, D. Jung. Brazeability of cold rolled three layer Al-7.5Si/Al-1.2Mn-2Zn-(0.04-1.0)Si/Al-7.5Si (wt%) clad sheets, *J. Mater. Process. Technol.* **130-131** (2002) 240-244.
9. D.M. Turriff, S.F. Corbin, M. Kozdras. Diffusional solidification phenomena in clad aluminum automotive braze sheet, *Acta Mater.* **58** (2010) 1332-1341.
10. D. A. Jones. "Principles and Prevention of Corrosion", Prentice Hall, 1996.
11. A.R. Lotz. Studien zur Nanostrukturierung von Aluminium-Oberflächen mittels elektrochemischer Methoden, PhD thesis, 2009.
12. K. P. Lee. Fabrication and Applications of Nanoporous Alumina Membranes, PhD thesis, 2013.
13. N. Birbilis, R.G. Buchheit. Electrochemical Characteristics of Intermetallic Phases in Aluminium Alloys, *J. Electrochem. Soc.* **152** (2005) B140-B151.
14. G.J. Marshall, R.K. Bolingbroke, A. Gray. Microstructural Control in an Aluminium Core Alloy for Brazing Sheet Applications, *Metall. Trans. A* **9** (1993) 1935 - 1942.
15. W.S. Miller, L. Zhuang, J. Bottema, A.J. Wittebrood, P. De Smet, A. Haszler, A. Vierregge. Recent development in aluminium alloys for the automotive industry, *Mater. Sci. and Eng. A* **280** (2000) 37-49.
16. G. Binnig, C.F. Quate, C. Gerber. Atomic force microscope, *Phys. Rev. Lett.* **56** (9) (1986) 930-933.

17. F.J. Giessibl. Atomic resolution on Si (111)-(7x7) by noncontact atomic force microscopy with a force sensor based on a quartz tuning fork, *Appl. Phys. Lett.* **76** (11) (2000) 1470-1472.
18. Q. Zhong, D. Inniss, K. Kjoller, V.B. Elings. Fractured polymer/silica ber surface studied by tapping mode atomic force microscopy, *Surf.Sci.Lett.* **290** (1-2) (1993) L688-L692.
19. N. F Martínez, R. García. Measuring phase shifts and energy dissipation with amplitude modulation atomic force microscopy, *Nanotechnology* **17** (2006) 167–172.
20. R. Garcia. "Amplitude Modulation Atomic Force Microscopy", Wiley-VCH Verlag GmbH & Co. KGaA, 2010.
21. S. Sadewasser, T. Glatzel. "Kelvin Probe Force Microscopy", Springer-Verlag Berlin Heidelberg, 2012.
22. J.S. Villarrubia. Morphological estimation of tip geometry for scanned probe microscopy, *Surf. Sci.* **321** (1994) 287-300.
23. H.O. Jacobs, P. Leuchtman, O.J. Homan, A. Stemmer. Resolution and contrast in Kelvin probe force microscopy, *J. Appl. Phys.* **84** (1998) 1168-1173.
24. T. Hochwitz, A.K. Henning, C. Levey, C. Daghljan. Capacitive effects on quantitative dopant profiling with scanned electrostatic force microscopes, *J. Vac. Sci. Technol. B* **14** (1996) 457-462.
25. O. Cherniavkaya, L. Chen, V. Weng, L. Yuditsky, I.E. Brus. Quantitative Noncontact Electrostatic Force Imaging of Nanocrystal Polarizability, *J. Phys. Chem. B* **107** (2003) 1525-1531.
26. S. Belaidi, P. Girard, G. Leveque. Electrostatic forces acting on the tip in atomic force microscopy: Modelization and comparison with analytic expressions, *J. Appl. Phys.* **81** (1997) 1023-1030.
27. L.Reimer, G.Pfefferkorn. "Raster-Elektronenmikroskopie", Springer-Verlag Berlin, 1977.
28. excitation volume SEM. SURF SEM EDX. <https://www.surfgroup.be/semedx>, June 2019.
29. P. Schmutz, G.S. Frankel. Characterization of AA2024-T3 by Scanning Kelvin Probe Force Microscopy, *J. Electrochem. Soc.* **145** (1998) 2285-2295.
30. ASTM Internatinal. ASTM G85: Standard Practice for Modified Salt Spray (Fog) Testing, 2002.
31. D. Nečas, P. Klapetek. Gwyddion: an open-source software for SPM data analysis. <http://gwyddion.net/>, February 2016.

32. F. Norouzi Afshar, A.M. Glenn, J.H.W. de Wit, H. Terryn, J.M.C. Mol. A combined electron probe micro analysis and scanning Kelvin probe force microscopy study of a modified AA4xxx/AA3xxx aluminium brazing sheet, *Electrochim. Acta* **104** (2013) 48-63.

## 7 Appendix

### 7.1 Results for AlSi10/Al99.85/AlZn4.5Mg1

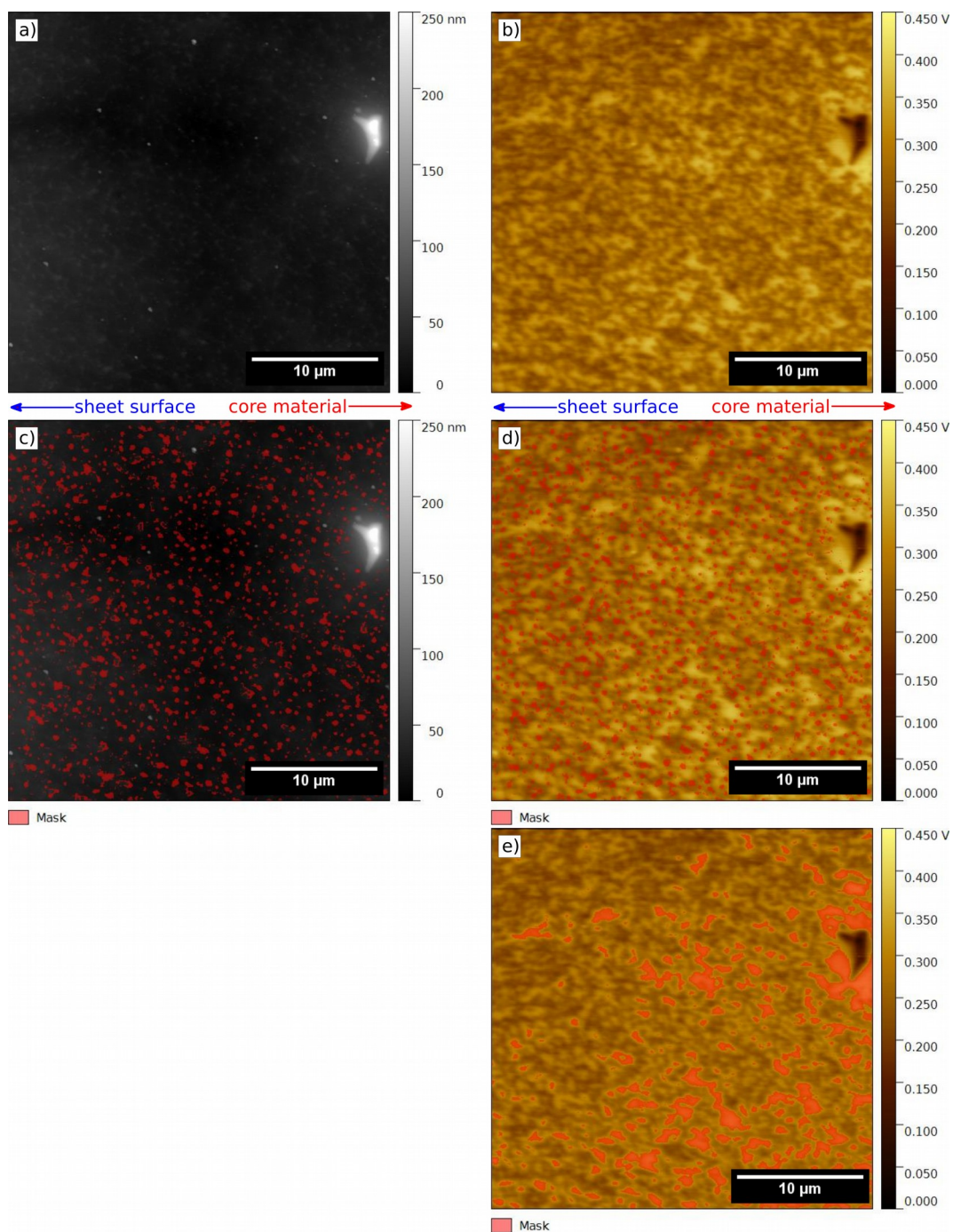


**Figure 7.1:** KPFM images for the border area of the 0 h sample. a) Topography and b) the corresponding CPD-map. c) The obtained mask of the topography map, which was then applied to the CPD-map d). e) Mask used for the matrix-CPD.

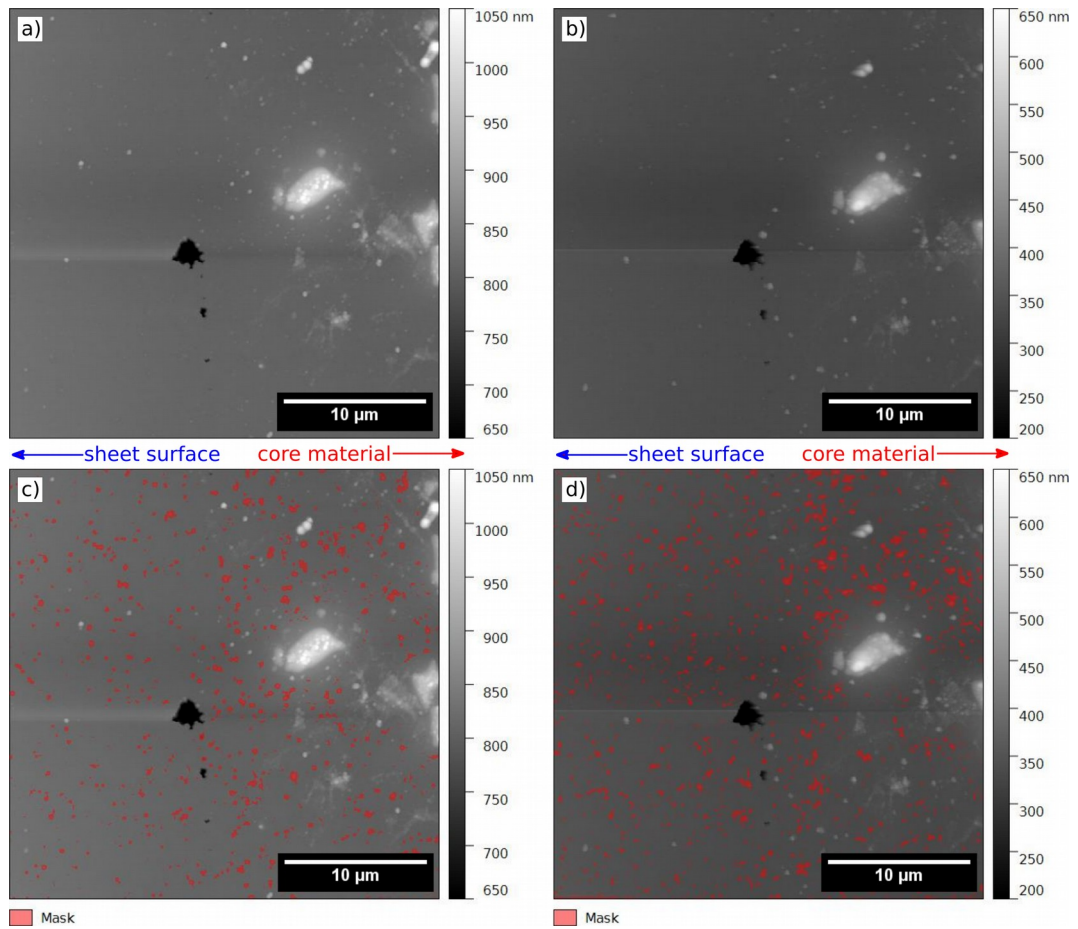


**Figure 7.2:** Topography images for the border area of the corrosion sample. a) Flattened topography for 1 h in the solution and b) flattened topography for 3 h. c) Mask for evaluation after 1 h immersion and d) after 3 h.

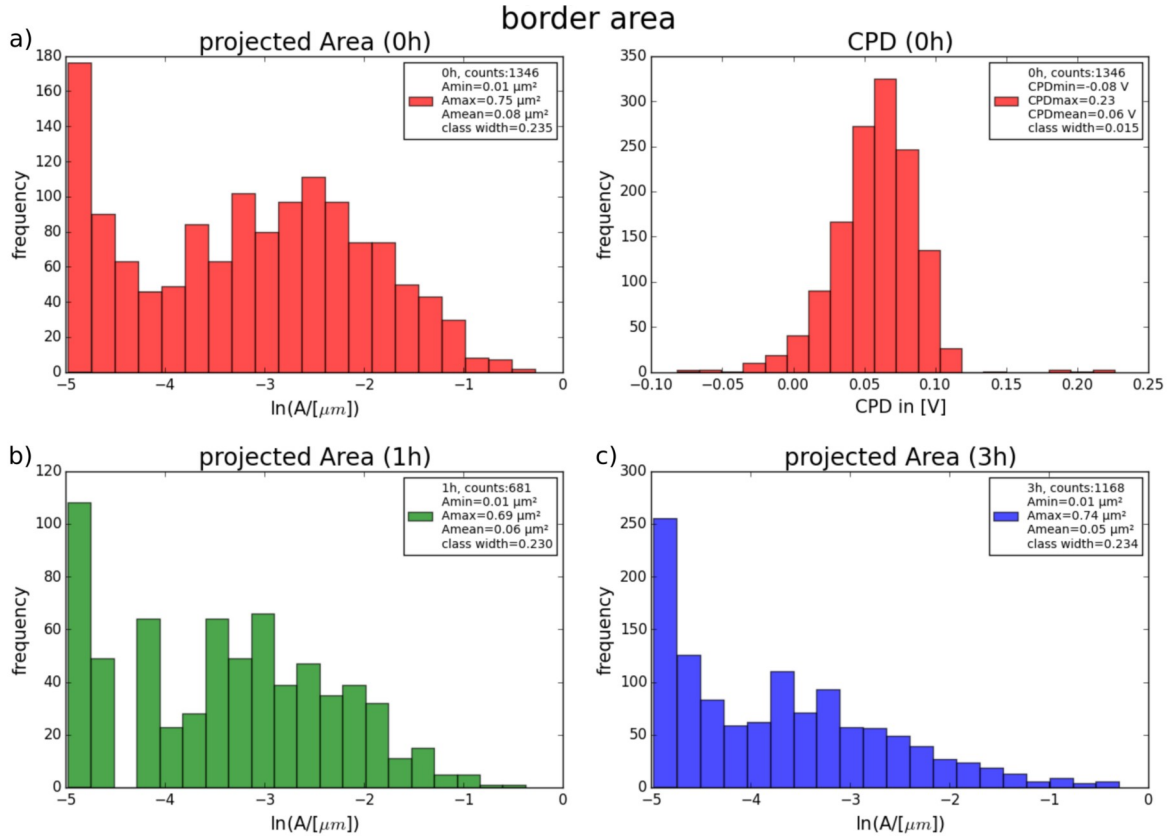


**Figure 7.3:** Results of the statistical evaluation of the projected area of the inclusions, as an indicator for their size, for the border area a) 0 h, b) 1 h and c) 3 h in solution. In a) additionally the CPD distribution is presented on the right. Counts in the legend is the total number of observed inclusions,  $A_{\min}$  is the smallest projected area of the analyzed inclusions ( $0.01 \mu\text{m}^2$  because of the resolution of the measurements), while  $A_{\max}$  is the largest.  $\text{CPD}_{\min}$  and  $\text{CPD}_{\max}$  refer to the highest difference between the measured inclusion CPD and the matrix-CPD value.

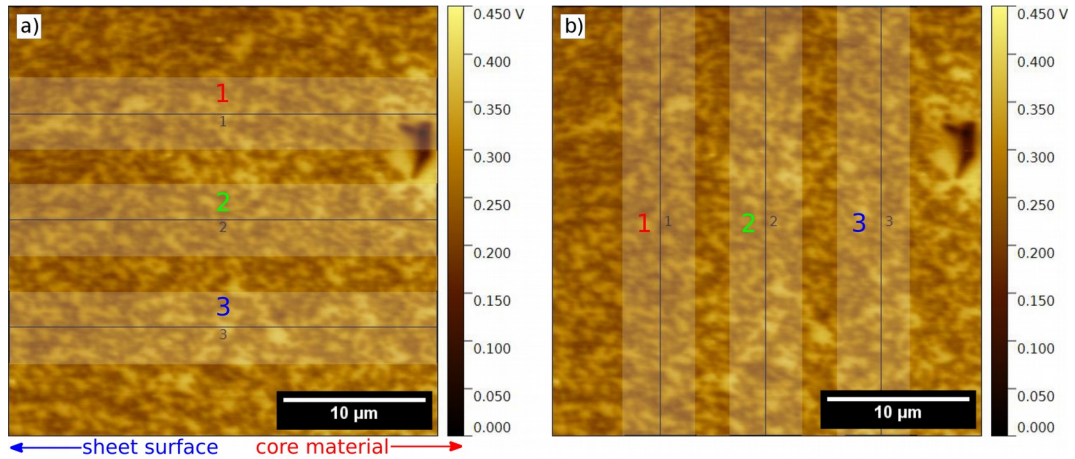


**Figure 7.4:** Direction dependent CPD-analysis of the KPFM image presented in Figure 7.1 b. a) Fast scan - b) slow scan direction. Semi-transparent white bars are used for width illustration, the numbers correspond to the lines presented in Figure 7.5.

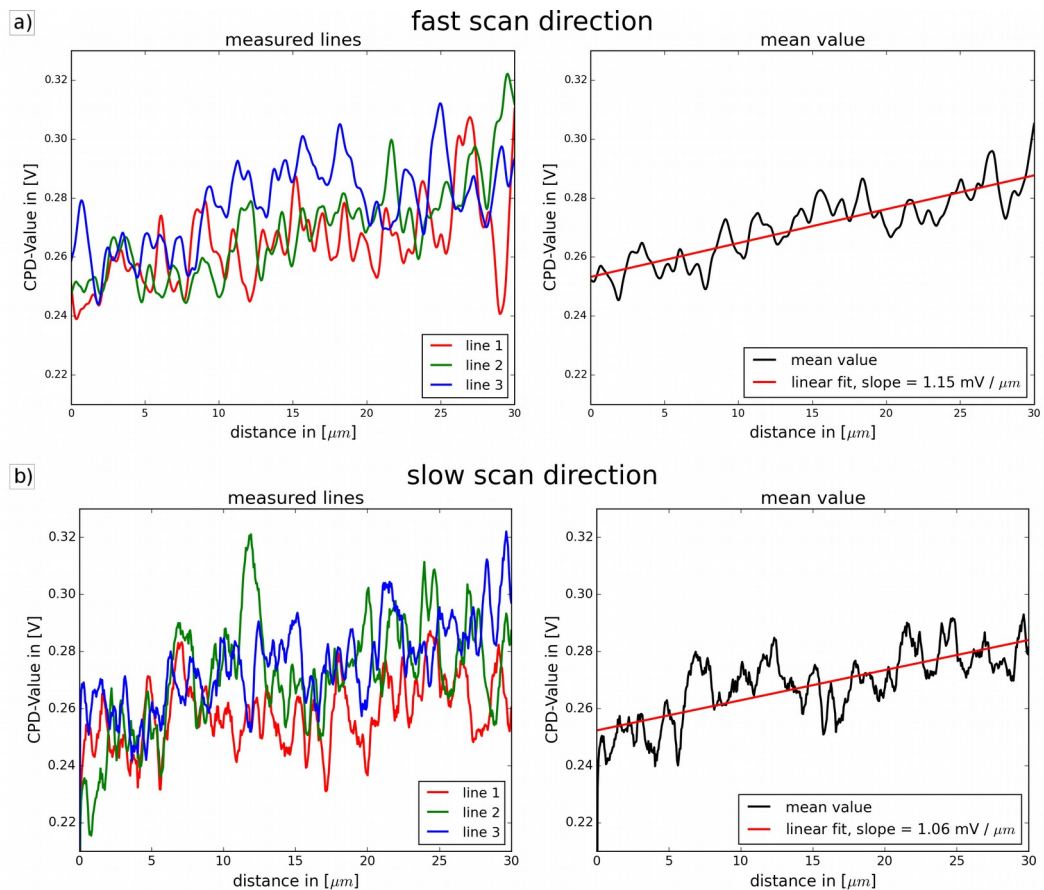


**Figure 7.5:** Line profiles extracted from the CPD-map seen in Figure 7.4. On the left side the originals are presented, a) in fast scan direction, b) in slow scan direction. On the right side, the mean values of the three extracted profiles are shown together with a linear fit and the resulting slope.

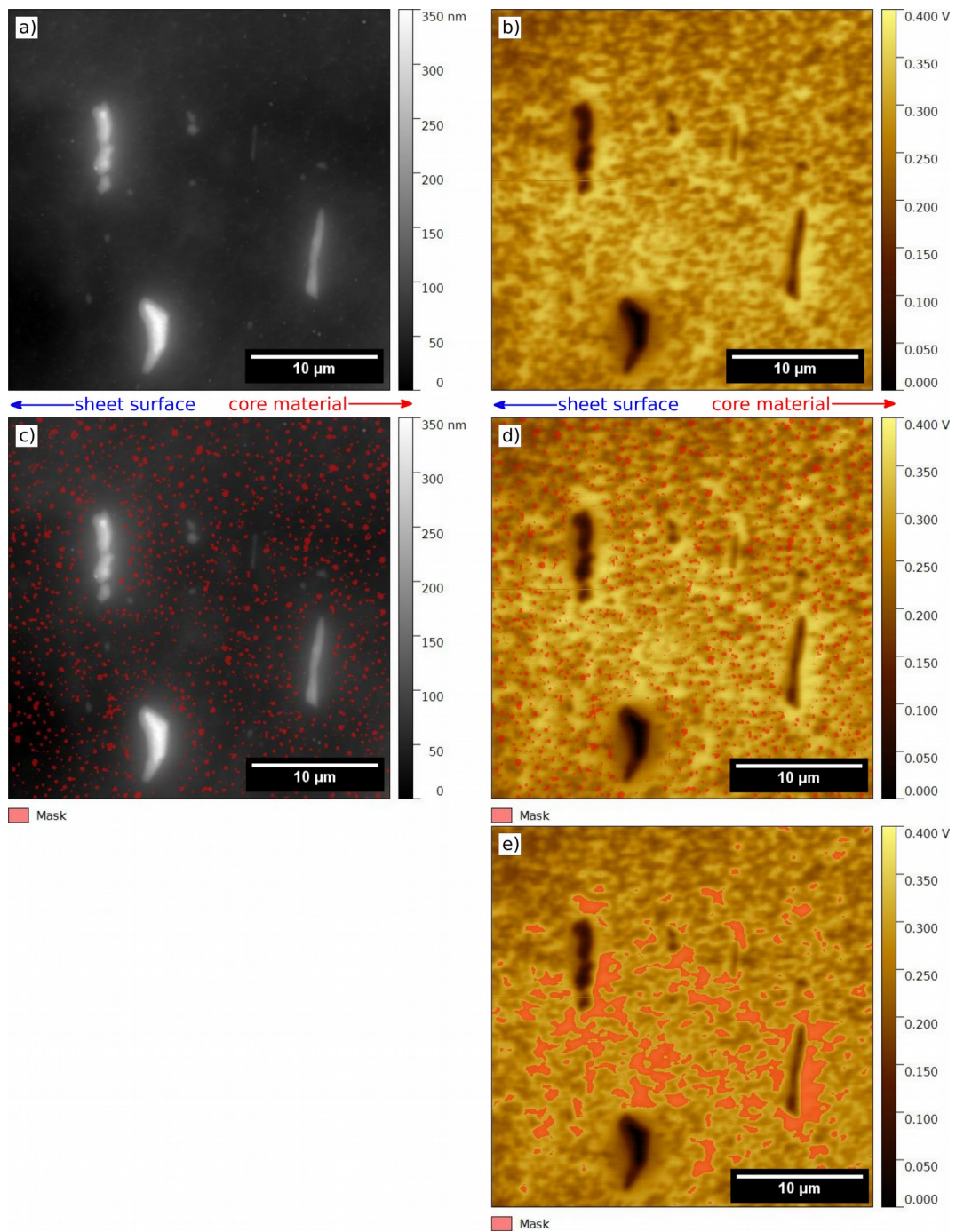


**Figure 7.6:** KPFM images for the core material of the 0 h sample. a) Topography and b) the corresponding CPD-map. c) The obtained mask of the topography map, which was then applied to the CPD-map d). e) Mask used for the matrix-CPD.



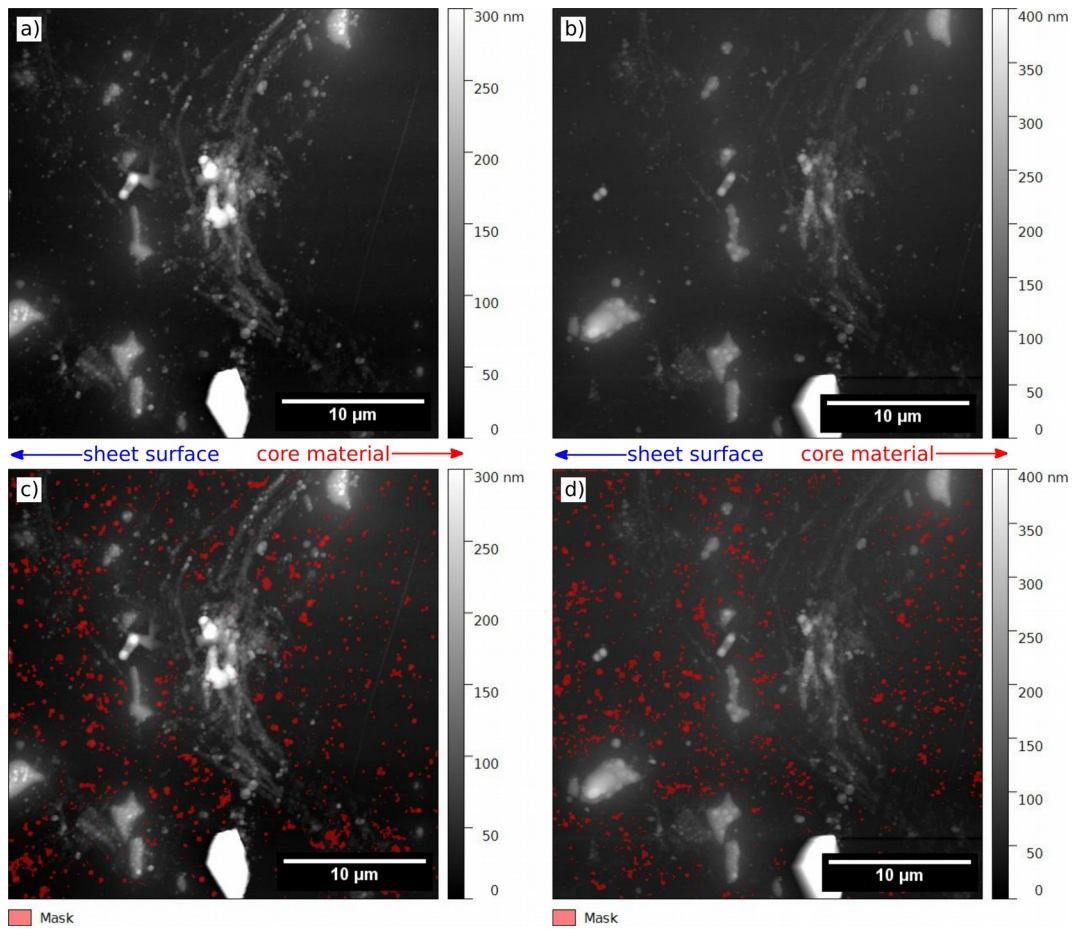


**Figure 7.7:** Topography images for the core material of the corrosion sample. a) Flattened topography for 1 h in the solution and b) flattened topography for 3 h. c) Mask for evaluation after 1 h immersion and d) after 3 h.

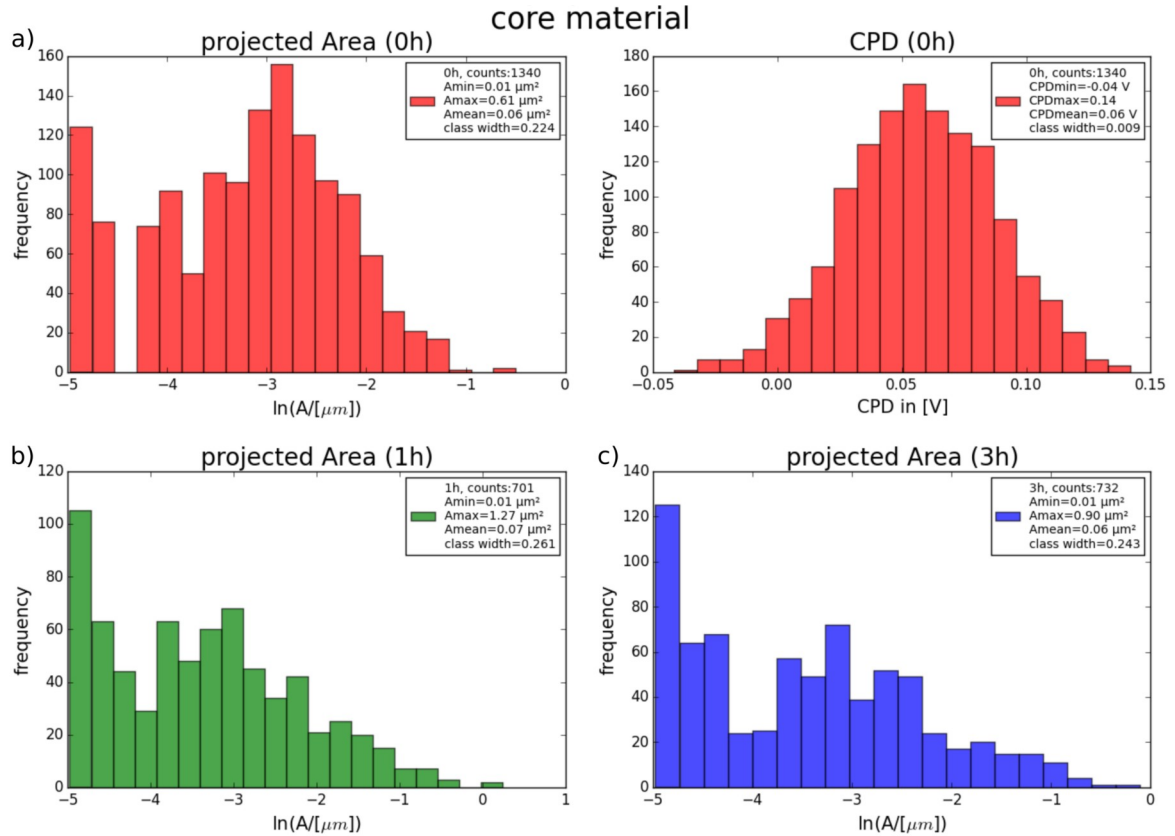


**Figure 7.8:** Results of the statistical evaluation of the projected area of the inclusions, as an indicator for their size, for the core material a) 0 h, b) 1 h and c) 3 h in solution. In a) additionally the CPD distribution is presented on the right. Counts in the legend is the total number of observed inclusions,  $A_{\min}$  is the smallest projected area of the analyzed inclusions ( $0.01 \mu\text{m}^2$  because of the resolution of the measurements), while  $A_{\max}$  is the largest.  $\text{CPD}_{\min}$  and  $\text{CPD}_{\max}$  refer to the highest difference between the measured inclusion CPD and the matrix-CPD value.

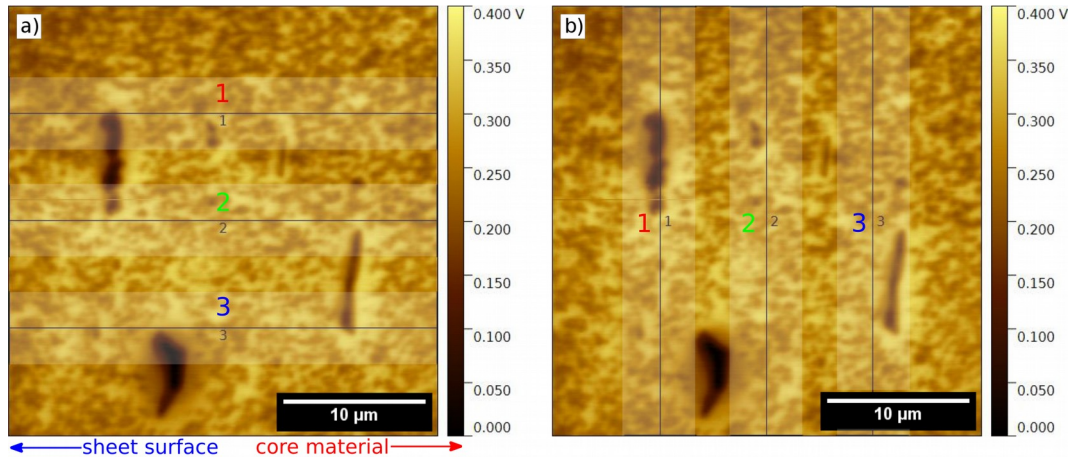


**Figure 7.9:** Direction dependent CPD-analysis of the KPFM image presented in Figure 7.6 b. a) Fast scan - b) slow scan direction. Semi-transparent white bars are used for width illustration, the numbers correspond to the lines presented in Figure 7.10.

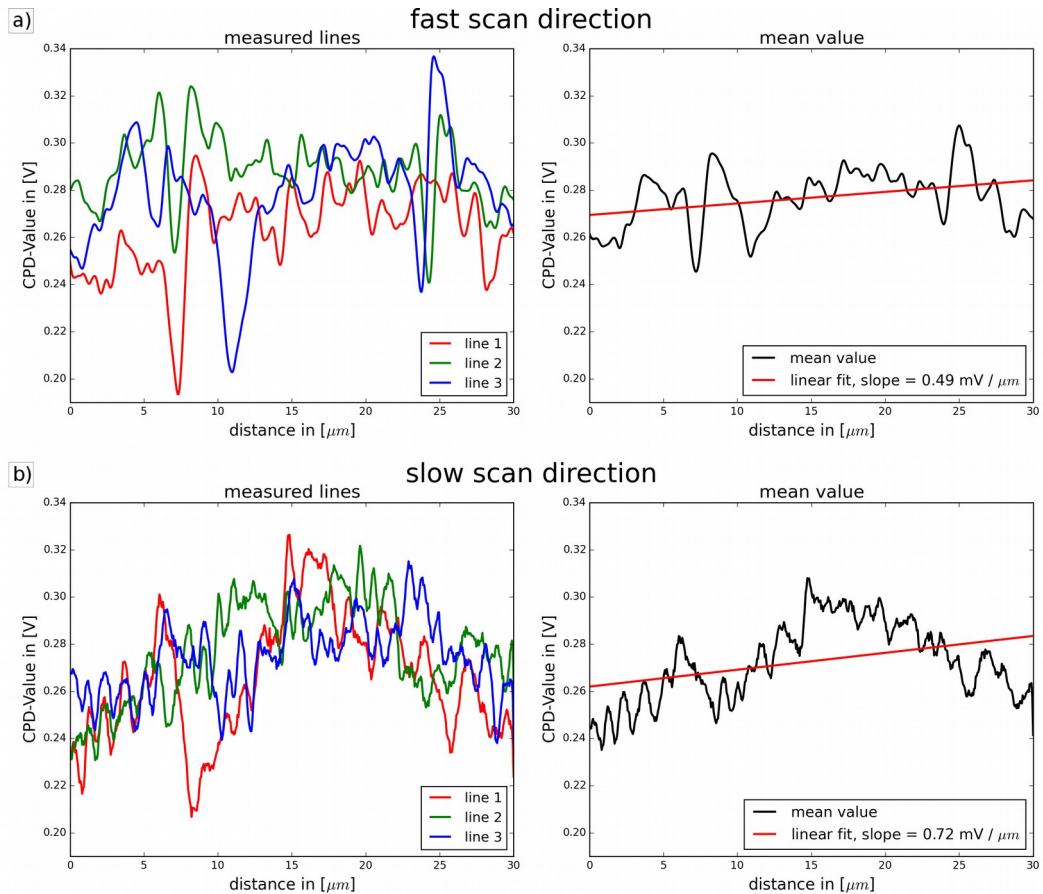


**Figure 7.10:** Line profiles extracted from the CPD-map seen in Figure 7.9. On the left side the originals are presented, a) in fast scan direction, b) in slow scan direction. On the right side, the mean values of the three extracted profiles are shown together with a linear fit and the resulting slope.

## 7.2 Python code to handle the AIMn1 Sample analysis

```
import matplotlib.pyplot as plt
import numpy as np
import pandas as pd

#loading of the 0h values from Gwyddion
t0 = pd.read_csv('0h/topo.txt', delimiter='\t')
v0 = pd.read_csv('0h/nap.txt', delimiter='\t') #\t = tabulator
m0 = pd.read_csv('0h/matrix.txt', delimiter='\t')
#looking for the extreme values; _b is on the border of the marked inclusion
t0['CPD_min'] = v0.z_min
t0['CPD_max'] = v0.z_max
t0['CPD_b_min'] = v0.b_min
t0['CPD_b_max'] = v0.b_max
t0['height'] = t0.z_max - t0.z_min
matrix0 = min(m0.z_min)
t0['CPD_diff'] = matrix0 - t0.CPD_min
t0['loch'] = t0.b_min - t0.z_min
#filtering for big inclusions
t0_gefiltert = t0[(t0.A_0 > 1e-12) & (t0.loch == 0) ]
#calculating the mean value and the standard deviation
ma0 = np.mean(t0_gefiltert.CPD_diff, dtype=np.float64)
staw0 = np.std(t0_gefiltert.CPD_diff, dtype=np.float64)
#plotting the CPD over projected area diagram
plt.hold(False)
plt.plot(t0_gefiltert.A_0 * 1e12, t0_gefiltert.CPD_diff, 'ro', markersize=7)
plt.ylabel('CPD-Difference in [V]', size=15)
plt.xlabel(u'projected area [ $\mu\text{m}^2$ ]', size=15)
plt.xticks(fontsize=10)
plt.yticks(fontsize=10)
plt.savefig("0h_CDP_A.png", dpi = 200)
#plotting the CPD over minimal diameter diagram
plt.plot(t0_gefiltert.D_min * 1e6, t0_gefiltert.CPD_diff, 'ro', markersize=7)
plt.ylabel('CPD-difference in [V]', size=15)
plt.xlabel(u'minimal diameter [ $\mu\text{m}$ ]', size=15)
plt.savefig("0h_CDP_D.png", dpi = 200)
#plotting the CPD over inscribed circle radius diagram
plt.plot(t0_gefiltert.R_i * 1e6, t0_gefiltert.CPD_diff, 'ro', markersize=7)
plt.ylabel('CPD-Difference in [V]', size=15)
```

```
plt.xlabel(u'inscribed circle radius in [ $\mu$  m$]', size=15)
plt.savefig ("0h_CDP_R.png", dpi = 200)
```

```
#same procedure for 1 h
```

```
t1 = pd.read_csv('1h/topo.txt', delimiter='\t')
v1 = pd.read_csv('1h/nap.txt', delimiter='\t')
m1 = pd.read_csv('1h/matrix.txt', delimiter='\t')
```

```
t1['CPD_min'] = v1.z_min
t1['CPD_max'] = v1.z_max
t1['CPD_b_min'] = v1.b_min
t1['CPD_b_max'] = v1.b_max
t1['height'] = t1.z_max - t1.z_min
matrix1 = min(m1.z_min)
t1['CPD_diff'] = matrix1 - t1.CPD_min
t1['loch'] = t1.b_min - t1.z_min
```

```
t1_gefilttert = t1[(t1.A_0 > 1e-12) & (t1.loch == 0) ]
ma1 = np.mean(t1_gefilttert.CPD_diff, dtype=np.float64)
staw1 = np.std(t1_gefilttert.CPD_diff, dtype=np.float64)
```

```
plt.plot(t1_gefilttert.A_0 * 1e12,t1_gefilttert.CPD_diff, 'ro', markersize=7)
plt.ylabel('CPD-Difference in [V]', size=15)
plt.xlabel(u'projected area [ $\mu$  m2]', size=15)
plt.savefig ("1h_CDP_A.png", dpi = 200)
```

```
plt.plot(t1_gefilttert.D_min * 1e6,t1_gefilttert.CPD_diff, 'ro', markersize=7)
plt.ylabel('CPD-Difference in [V]', size=15)
plt.xlabel(u'minimal diameter [ $\mu$  m$]', size=15)
plt.savefig ("1h_CDP_D.png", dpi = 200)
```

```
plt.plot(t1_gefilttert.R_i * 1e6,t1_gefilttert.CPD_diff, 'ro', markersize=7)
plt.ylabel('CPD-Difference in [V]', size=15)
plt.xlabel(u'inscribed circle radius in [ $\mu$  m$]', size=15)
plt.savefig ("1h_CDP_R.png", dpi = 200)
```

```

#same procedure for 3 h
t3 = pd.read_csv('3h/topo.txt', delimiter='\t')
v3 = pd.read_csv('3h/nap.txt', delimiter='\t')
m3 = pd.read_csv('3h/matrix.txt', delimiter='\t')

t3['CPD_min'] = v3.z_min
t3['CPD_max'] = v3.z_max
t3['CPD_b_min'] = v3.b_min
t3['CPD_b_max'] = v3.b_max
t3['height'] = t3.z_max - t3.z_min
matrix3 = min(m3.z_min)
t3['CPD_diff'] = matrix3 - t3.CPD_min
t3['loch'] = t3.b_min - t3.z_min

t3_gefilttert = t3[(t3.A_0 > 1e-12) & (t3.loch == 0)]
ma3 = np.mean(t3_gefilttert.CPD_diff, dtype=np.float64)
staw3 = np.std(t3_gefilttert.CPD_diff, dtype=np.float64)

plt.plot(t3_gefilttert.A_0 * 1e12, t3_gefilttert.CPD_diff, 'ro', markersize=7)
plt.ylabel('CPD-Difference in [V]', size=15)
plt.xlabel(u'projected Area [ $\mu\text{m}^2$ ]', size=15)
plt.savefig("3h_CDP_A.png", dpi = 200)

plt.plot(t3_gefilttert.D_min * 1e6, t3_gefilttert.CPD_diff, 'ro', markersize=7)
plt.ylabel('CPD-Difference in [V]', size=15)
plt.xlabel(u'minimal Diameter [ $\mu\text{m}$ ]', size=15)
plt.savefig("3h_CDP_D.png", dpi = 200)

plt.plot(t3_gefilttert.R_i * 1e6, t3_gefilttert.CPD_diff, 'ro', markersize=7)
plt.ylabel('CPD-Difference in [V]', size=15)
plt.xlabel(u'inscribed circle radius in [ $\mu\text{m}$ ]', size=15)
plt.savefig("3h_CDP_R.png", dpi = 200)

```

```

#same procedure for 9 h
t9 = pd.read_csv('9h/topo.txt', delimiter='\t')
v9 = pd.read_csv('9h/nap.txt', delimiter='\t')
m9 = pd.read_csv('9h/matrix.txt', delimiter='\t')

t9['CPD_min'] = v9.z_min
t9['CPD_max'] = v9.z_max
t9['CPD_b_min'] = v9.b_min
t9['CPD_b_max'] = v9.b_max
t9['height'] = t9.z_max - t9.z_min
matrix9 = min(m9.z_min)
t9['CPD_diff'] = matrix9 - t9.CPD_min
t9['loch'] = t9.b_min - t9.z_min

t9_gefiltert = t9[(t9.A_0 > 1e-12) & (t9.loch == 0)]
ma9 = np.mean(t9_gefiltert.CPD_diff, dtype=np.float64)
staw9 = np.std(t9_gefiltert.CPD_diff, dtype=np.float64)

plt.plot(t9_gefiltert.A_0 * 1e12, t9_gefiltert.CPD_diff, 'ro', markersize=7)
plt.ylabel('CPD-Difference in [V]', size=15)
plt.xlabel(u'projected Area [ $\mu\text{m}^2$ ]', size=15)
plt.savefig("9h_CDP_A.png", dpi = 200)

plt.plot(t9_gefiltert.D_min * 1e6, t9_gefiltert.CPD_diff, 'ro', markersize=7)
plt.ylabel('CPD-Difference in [V]', size=15)
plt.xlabel(u'minimal Diameter [ $\mu\text{m}$ ]', size=15)
plt.savefig("9h_CDP_D.png", dpi = 200)

plt.plot(t9_gefiltert.R_i * 1e6, t9_gefiltert.CPD_diff, 'ro', markersize=7)
plt.ylabel('CPD-Difference in [V]', size=15)
plt.xlabel(u'inscribed circle radius in [ $\mu\text{m}$ ]', size=15)
plt.savefig("9h_CDP_R.png", dpi = 200)

```

```

#plotting the diagram for the CPD mean values over time in solution
me = [ma0, ma1, ma3, ma9]
staw = [staw0, staw1, staw3, staw9]
time = [0, 1, 3, 9]

plt.plot(time,me,'b-')
plt.errorbar(time,me,yerr = staw ,linewidth=2, elinewidth=1.5,capthick=1.5, ecolor='r')
plt.xlabel('time in solution [h]', size=15)
plt.ylabel('CPD-Difference in [V]', size=15)
plt.xlim(-1,10)
plt.savefig ("CPDOverTime", dpi = 200)

#plotting maps to control the filter parameters
plt.plot(t0_gefiltert.x_c*1e6,-t0_gefiltert.y_c*1e6,'r+')
plt.xlim(0,30)
plt.ylim(-30,0)
plt.axes().set_aspect('equal')
plt.savefig ("0hLocation",transparent = True, dpi = 200)

plt.plot(t1_gefiltert.x_c*1e6,-t1_gefiltert.y_c*1e6,'r+')
plt.xlim(0,30)
plt.ylim(-30,0)
plt.axes().set_aspect('equal')
plt.savefig ("1hLocation",transparent = True, dpi = 200)

plt.plot(t3_gefiltert.x_c*1e6,-t3_gefiltert.y_c*1e6,'r+')
plt.xlim(0,30)
plt.ylim(-30,0)
plt.axes().set_aspect('equal')
plt.savefig ("3hLocation",transparent = True, dpi = 200)

plt.plot(t9_gefiltert.x_c*1e6,-t9_gefiltert.y_c*1e6,'r+')
plt.xlim(0,30)
plt.ylim(-30,0)
plt.axes().set_aspect('equal')
plt.savefig ("9hLocation",transparent = True, dpi = 200)

```